Cell Reports

Article

Cerebral organoids derived from patients with Alzheimer's disease with PSEN1/2 mutations have defective tissue patterning and altered development

Graphical abstract

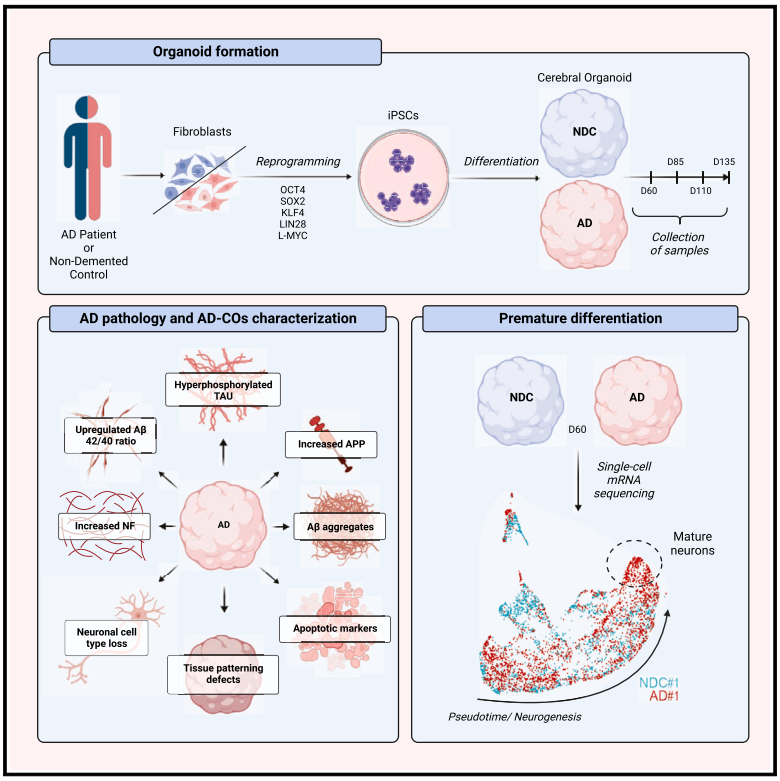

Highlights

- Cerebral organoids generated from patients with fAD forms develop AD-like pathology
- AD organoids react to β- and γ-secretase inhibitors by decreasing levels of Aβ peptides
- AD organoids show developmental and tissue patterning defects
- Single-cell-seq data support altered development and the signs of premature differentiation

Authors

Tereza Vanova, Jiri Sedmik, Jan Raska, ..., Zdenek Spacil, Hana Hribkova, Dasa Bohaciakova

Correspondence

bohaciakova@med.muni.cz

In brief

Vanova et al. show that brain organoids differentiated from induced pluripotent stem cells with mutations in *PSEN1* and *PSEN2* genes mimic the development of Alzheimer's disease-like pathology *in vitro*. Curiously, these brain organoids also exhibit developmental and tissue patterning defects, supported by mRNA single-cell sequencing data showing premature neuronal differentiation.

Vanova et al., 2023, Cell Reports *42*, 113310
November 28, 2023
https://doi.org/10.1016/j.celrep.2023.113310

CellPress

Cell Reports

CellPress
OPEN ACCESS

Article

Cerebral organoids derived from patients with Alzheimer's disease with PSEN1/2 mutations have defective tissue patterning and altered development

Tereza Vanova,[1,2] Jiri Sedmik,[1] Jan Raska,[1,2] Katerina Amruz Cerna,[1] Petr Taus,[3] Veronika Pospisilova,[1] Marketa Nezvedova,[4] Veronika Fedorova,[1] Sona Kadakova,[1] Hana Klimova,[1] Michaela Capandova,[1] Petra Orviska,[1] Petr Fojtik,[1,2] Simona Bartova,[1] Karla Plevova,[3,5] Zdenek Spacil,[4] Hana Hribkova,[1] and Dasa Bohaciakova[1,2,6,*]

[1]Department of Histology and Embryology, Faculty of Medicine, Masaryk University, 62500 Brno, Czech Republic
[2]International Clinical Research Center (ICRC), St. Anne's University Hospital, 60200 Brno, Czech Republic
[3]Central European Institute of Technology, Masaryk University, 62500 Brno, Czech Republic
[4]RECETOX, Faculty of Science, Masaryk University, 62500 Brno, Czech Republic
[5]Institute of Medical Genetics and Genomics, University Hospital Brno and Faculty of Medicine, Masaryk University, 61300 Brno, Czech Republic
[6]Lead contact
*Correspondence: bohaciakova@med.muni.cz
https://doi.org/10.1016/j.celrep.2023.113310

SUMMARY

During the past two decades, induced pluripotent stem cells (iPSCs) have been widely used to study human neural development and disease. Especially in the field of Alzheimer's disease (AD), remarkable effort has been put into investigating molecular mechanisms behind this disease. Then, with the advent of 3D neuronal cultures and cerebral organoids (COs), several studies have demonstrated that this model can adequately mimic familial and sporadic AD. Therefore, we created an AD-CO model using iPSCs derived from patients with familial AD forms and explored early events and the progression of AD pathogenesis. Our study demonstrated that COs derived from three AD-iPSC lines with *PSEN1*(A246E) or *PSEN2*(N141I) mutations developed the AD-specific markers *in vitro*, yet they also uncover tissue patterning defects and altered development. These findings are complemented by single-cell sequencing data confirming this observation and uncovering that neurons in AD-COs likely differentiate prematurely.

INTRODUCTION

Alzheimer's disease (AD) is an incurable, progressive neurodegenerative disorder characterized by severe loss of neurons in the cerebral cortex and subsequent cortical dysfunction. Familial AD (fAD) cases are most commonly caused by mutations in amyloid precursor protein (*APP*) and presenilin 1 and 2 (*PSEN1* and *PSEN2*) genes, while allele 4 of apolipoprotein E (*APOE4*) represents one of the risk factors associated with sporadic AD (sAD). Clinically, AD is underlaid by extracellular β-amyloid (Aβ) plaques formed by accumulating insoluble deposits of Aβ peptides cleaved from APP and by neurofibrillary tangles and intraneuronal aggregates of hyperphosphorylated microtubule-associated protein Tau (P-Tau). Additionally, Aβ42 and Aβ40 peptides are also being secreted, and the Aβ42/40 ratio detected in the cerebrospinal fluid (CSF) is a well-established clinical marker of ongoing neurodegeneration in patients with AD.[1] Besides Aβ and P-Tau, other AD-related hallmarks include an increased level of neurofilament-light (NF-L) chain in CSF,[2] loss of cholinergic neurons in the basal forebrain,[3] and upregulation of markers of cellular stress and senescence.[4,5] Importantly, the manifestation of cognitive decline in patients with AD is preceded by a long preclinical phase, with the entire disease process likely spanning more than 20 years.[6] Thus, to uncover mechanisms leading to AD, it is essential to study models that allow for investigating the early stages of human AD development.

Induced pluripotent stem cells (iPSCs) have previously been proven to be such a model system, as they can be obtained from somatic cells of patients with AD, differentiated to disease-relevant cell types, and subsequently used to (1) test mechanisms of disease initiation and progression, (2) screen for potential drugs, or (3) evaluate functional roles of genetic mutations during the disease development *in vitro*.[7] Indeed, numerous reports based on 2D cell culture models have already provided new clues about changes in neuronal development, physiology, and functions associated with AD (reviewed in Barak et al.[8]). Naturally, with the advent of 3D neuronal/stem cell culture systems that better reflect the cerebral complexity found *in vivo*, a number of studies have reported the establishment of these models for both sAD[9,10] and fAD[11,12] (reviewed in Barak et al.[8]). These reports show that stem cell-based 3D models increase the formation of Aβ-plaque-like aggregates and increase the phosphorylation of Tau protein. Most of them also demonstrate that AD-associated markers could be ameliorated

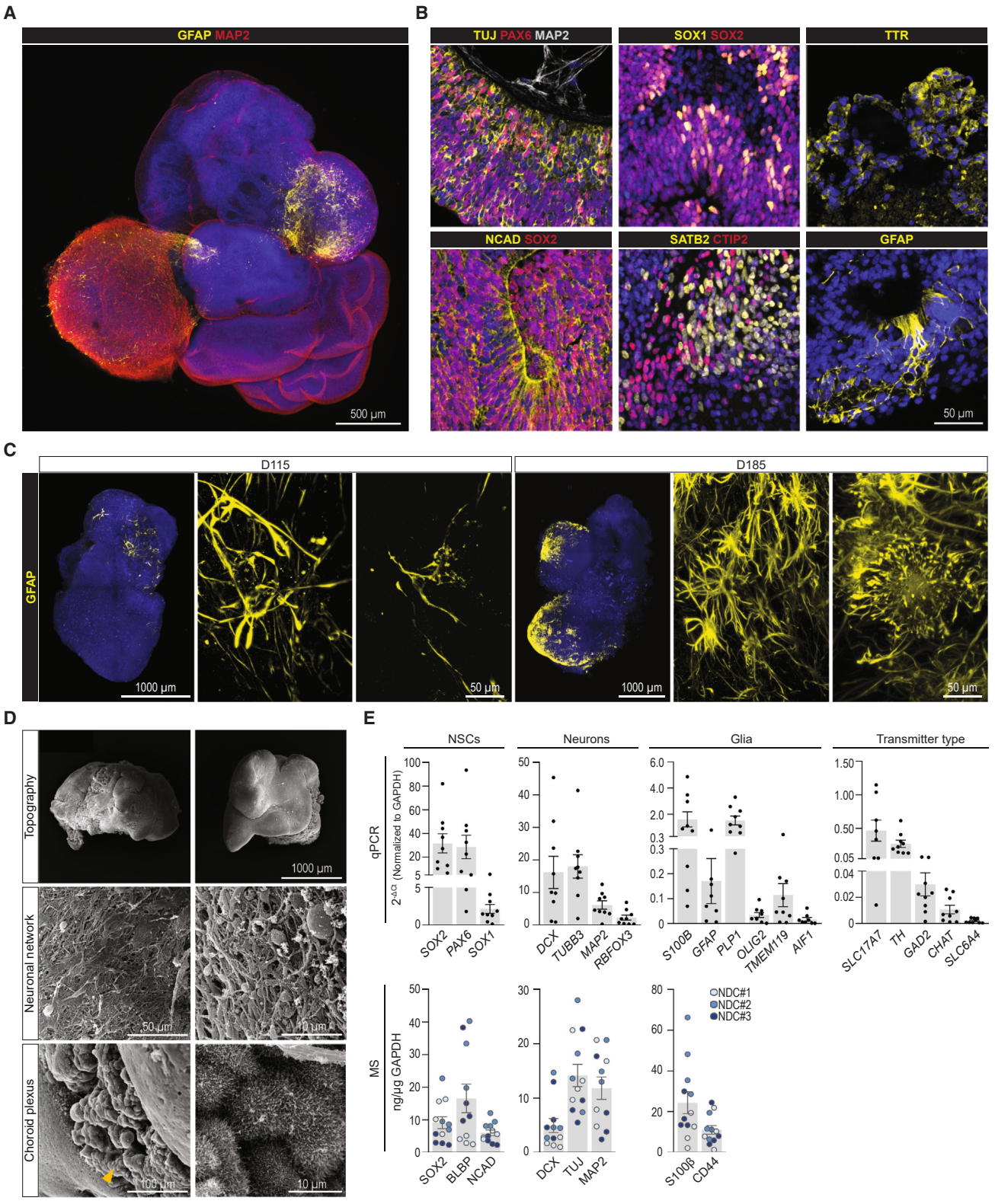

Figure 1. Human NDC-iPSC-derived COs show mature morphology and neuronal and glial marker expression

(A–D) Representative images depicting CO morphology.

(A) Whole-mount staining of CO at D145 (GFAP astrocytes, MAP2 neurons).

(legend continued on next page)

by β- or γ-secretase inhibitors, providing functional proof that these models could be used for drug screening. However, the potential of 3D stem cell-based models remains largely unexplored, as this system could provide significant clues to the cellular and molecular changes coupled to not only existing AD markers but also uncover the dynamics of their development. Importantly, as increasing evidence show that early alterations in brain development contribute to the manifestation of neurodegenerative diseases later in life,[13] they could also reveal the initial steps of AD.

Here, we created such a model to address underlying mechanisms and dynamics leading to AD development *in vitro*. We report the establishment of an AD-iPSC-based model of cerebral organoids (COs) and provide a characterization of over 700 COs derived from three patients with fAD, carriers of *PSEN1*(A246E)[14] or *PSEN2*(N141I)[15,16] mutations, and their complementary age- and sex-matched control iPSCs and one isogenic pair of iPSCs carrying *PSEN1*(A246E) mutation. We show that *PSEN1/2* mutant organoids form diffuse- and compact-like Aβ aggregates that increase in size as organoids age *in vitro*. This accumulation is accompanied by an increased Aβ42/40 ratio of secreted Aβ peptides. Additionally, we detected other AD-related markers, including P-TAU (Ser202/Thr205), and a trend toward increased expression of NFs and a lower expression of *CHAT*+ cholinergic neurons. AD-COs also exhibit ongoing cellular stress/apoptosis and senescence. Importantly, we demonstrate that despite similar expression of cell-type-specific genes during CO maturation, AD-iPSC-derived COs showed limited tissue patterning and altered cellular development. These findings are complemented with single-cell sequencing data of AD-COs, confirming this observation and demonstrating that neurons in AD-iPSCs likely differentiate prematurely.

RESULTS

Human iPSC-derived COs differentiated from non-demented controls show mature morphology, complex patterning, and neuronal and glial marker expression

To initiate our studies, we generated a panel of iPSC lines from three individuals with fAD (here referred to as AD#1–3) and three complementary (sex-, age-, and *APOE*-status-matched) non-demented control (NDC) subjects (here referred to as NDC#1–3; listed in Figure S1A). A set of AD-iPSC lines consisted of two independent cell lines with *PSEN1*(A246E) mutation (AD#1, AD#2) and a third cell line with *PSEN2*(N141I) mutation (AD#3). AD#1 and AD#2 then differed in *APOE* status, with the AD#1 line carrying the *E3/3* and the AD#2 line carrying the *E3/4* genotype. All six derived iPSC lines were previously characterized[17] and registered at the Human Pluripotent Stem Cell Registry (https://hpscreg.eu).

To generate COs, we first optimized the protocol on healthy NDC-iPSC lines. We followed previously published protocol[18] with minor modifications described in STAR Methods. COs showed typical morphology during their development (Figure S1B), starting with smooth round spheroids in the Neuroinduction medium (day 9), followed by the expansion of neuroepithelium in a Geltrex scaffold (day 15) and significant growth and maturation at later stages of CO development (days 45–80). Some NDC-COs formed structures resembling choroid plexus (day 45) and, later in development, also exhibited pigmented areas (day 80). Morphological characterization confirmed expression of neuronal (microtubule-associated protein 2 [MAP2]) and astrocytic (glial fibrillary acidic protein [GFAP]) markers as visualized using whole-mount staining (Figure 1A). In tissue sections (Figure 1B), we detected the expression of markers typical for neural stem cells (NSCs; SOX2, SOX1, PAX6, N-cadherin [NCAD]), neurons (doublecortin [DCX], β-Tubulin 3 [TUJ], MAP2, NeuN, NF-L, synapsin-1 [SYN1], SATB2, CTIP2), astrocytes (GFAP), and choroid plexus (transthyretin [TTR]) (Figures 1B and S1C). Importantly, their localization, and often a mutual exclusion of these markers, confirmed a high degree of tissue organization in healthy NDC-COs. Additionally, our data confirmed that COs gradually developed morphologically different astrocytic subtypes, and their number also progressively increased with age (Figure 1C). Lastly, these observations were complemented using scanning electron microscopy (SEM; Figure 1D), showing the topography of intact COs and complex neuronal networks and choroid-plexus-like structures on their surface.

We then used quantitative methods to characterize the NDC-COs at day 85 in greater detail (Figure 1E). Using qPCR of pooled CO samples (5–9 COs per sample) derived from three independent differentiation batches of three NDC-iPSC lines (n = 9), we detected the expression of NSC markers (*SOX2*, *SOX1*, *PAX6*), markers of immature and mature neurons (*DCX*, *TUBB3*/TUJ, *MAP2*, *RBFOX3*/NeuN), and glia (astrocytes: *S100B*, *GFAP*; oligodendrocytes: *PLP1*, *OLIG2*; microglia: *TMEM119*, *AIF1*/ionized calcium binding adapter protein 1 [IBA1]). Exploration of neuronal subtypes revealed that NDC-COs express markers of glutamatergic (*SLC17A7*/vesicular glutamate transporter [vGLUT]), dopaminergic (*TH*), GABAergic (*GAD2*), cholinergic (*CHAT*), and serotonergic (*SLC6A4*/serotonin transporter [SERT]) neurons. Additionally, some of the cell-type-specific markers (i.e., progenitor/radial glia: SOX2, brain lipid-binding protein [BLBP]/*FABP7*, NCAD; neurons: DCX, TUJ, MAP2; glia: S100β, CD44) were also detected on a protein level using

(B) Paraffin sections of COs (days 60–85) showing localization of NSCs/neuroectoderm (PAX6, SOX1, SOX2, NCAD), neuronal (TUJ, MAP2, SATB2, CTIP2), astrocytic (GFAP), and choroid plexus (TTR) markers.
(C) Whole-mount staining of COs at days 115 (left) and 185 (right) depicting the amount of GFAP-positive astrocytes. High-magnification images show the morphology of different astrocyte subtypes developed over time.
(D) Topography of whole organoids (day 75; top) and details of neuronal network (middle) and choroid plexus (bottom, marked with yellow arrow) visualized by SEM.
(E) qPCR (top) and mass spectrometry (MS) (bottom) analysis of cell-type-specific markers in day 85 organoids differentiated from NDC#1, NDC#2, and NDC#3 cell lines. Each dot in the qPCR graphs represents a pooled sample of 5–9 COs (n = 9), and the data are presented as $2^{-\Delta Ct}$ normalized to GAPDH. Each color-coded dot in the MS graphs represents a single organoid (n = 12). Error bars represent SEM.
See also Figure S1 and Table S1.

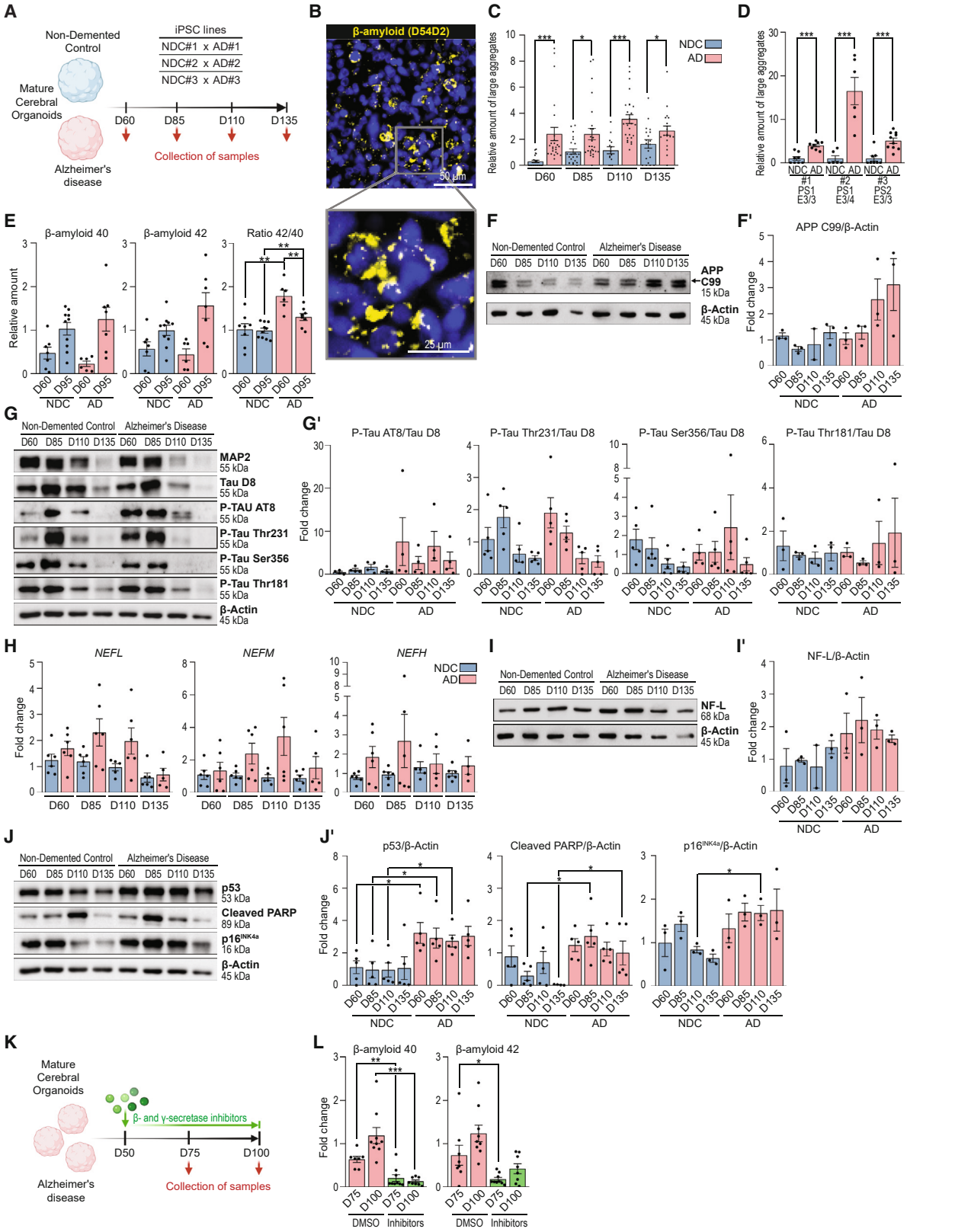

(legend on next page)

targeted mass spectrometry (MS) analysis. Importantly, this highly sensitive analysis allowed us to determine the expression of each marker in single COs. We thus analyzed four independent organoids from each NDC-iPSC line (n = 12). This revealed that all three NDC-iPSC lines have a similar capacity to differentiate, and the observed heterogeneity of marker expression is primarily due to variability between COs within one differentiation batch. Thus, our initial experiments confirm that mature COs derived from three newly established NDC-iPSC lines have typical organoid morphology and a high degree of tissue organization and express typical neuronal and glial markers.

Organoids derived from AD-iPSCs develop AD-related markers

To evaluate the ability of our model to develop AD-related markers, we compared the COs derived from AD- and NDC-iPSCs. As schematized in Figure 2A, all six iPSC lines were differentiated toward mature COs and collected in four time points during maturation (days 60, 85, 110, and 135) to evaluate the dynamics of the development of AD-specific markers. First, we analyzed the accumulation and cleavage of APP and the secretion of Aβ. Figure 2B shows a representative image of the Aβ signal at day 85, where the accumulation of Aβ is detected on the histological sections of AD-COs. The size of the Aβ signal ranged from small particles to large aggregates reminiscent of diffuse- and compact-like plaques found in patients with AD.[19] Notably, the quantification of the size of these Aβ aggregates in each time point revealed that the relative amount of large Aβ aggregates was already significantly higher in all AD-COs at day 60, and it gradually increased over time (Figure 2C). It is of note that the size of Aβ aggregates also increased in control NDC-COs with aging, albeit to a lower extent. When we compared the size at day 60 between individual iPSC lines, we detected the highest amount of Aβ aggregates in organoids derived from the AD#2 cell line carrying an *APOE3/4* risk genotype on the background of *PSEN1*(A246E) mutation (Figure 2D). Results were also complemented by western blot (WB) analysis, which showed a higher level of total APP in the cell lysates of AD-COs in comparison to NDC-COs (Figures S2A and S2A′). Finally, we assessed the amount of Aβ40 and Aβ42 peptides secreted in the cell culture medium using ELISA and detected a significantly upregulated Aβ42/40 ratio in AD-COs compared with NDC-COs at two analyzed time points (day 60 and 95; Figure 2E). Additionally, several lines of recent evidence indicate that that the C-terminal fragments derived from APP (APP-CTFs) might be linked to the initial cause of AD pathology.[20] Consequently, we examined the C99 fragment and observed a progressive rise in its concentration over time, specifically in AD-COs (Figures 2F and 2F′). These data confirm that APP accumulation, cleavage, and Aβ secretion are triggered in our AD-COs with mutations in *PSEN1* and *PSEN2*.

We subsequently aimed to detect other AD-related markers, including P-Tau, increased expression of NFs, neuronal cell type loss, increased cellular stress/apoptosis, and induction of senescence. To evaluate the P-Tau, we used a set of antibodies raised against a panel of P-Tau epitopes. Out of four tested antibodies, the AT8 antibody showed a trend toward higher phosphorylation of Ser202/Thr205 residues in AD-COs (Figures 2G and G′). A similar trend was observed for the expression of NFs. Both qPCR (Figure 2H) and protein analysis using WB (Figures 2I and 2I′) and targeted MS (Figure S2B) confirmed the tendency toward a higher expression of NF-L (*NEFL*), -medium (*NEFM*/NF-M), and -heavy (*NEFH*) chains in AD-COs. Gene expression analysis of five neuronal subtypes revealed that only the marker of cholinergic neurons (*CHAT*) shows a trend toward lower expression in AD-COs (Figure S2C). Finally, we also analyzed the extent of cellular stress/apoptosis and senescence. Despite the substantial heterogeneity of COs, we detected significantly upregulated levels of p53 and cleaved PARP (markers of cellular stress/apoptosis; C-PARP) and $p16^{INK4a}$ (a senescence marker) in AD-COs (Figures 2J and 2J′).

Figure 2. Organoids derived from AD-iPSCs gradually develop the AD-related markers

(A) Experimental scheme depicting days of sample collection (days 60, 85, 110, and 135) of NDC (NDC#1, NDC#2, and NDC#3; blue) and AD (AD#1, AD#2, and AD#3; red) COs.

(B) Representative immunofluorescent image of Aβ aggregates in the histological section of AD-CO (day 85).

(C and D) Quantification of Aβ aggregates measured as a percentage of large aggregates detected in COs. Each dot represents pooled data from 4 to 6 images from one histological section. (C) Aβ accumulation during CO differentiation of all six iPSC lines at all analyzed time points (NDC: n = 6, AD: n = 6) and (D) individual cell lines at day 60 (NDC: n = 6, AD: n = 6). Data were normalized to the average of the respective NDC-COs.

(E) Quantification of Aβ40 and Aβ42 peptides secreted into media (measured by ELISA) and the resulting Aβ42/40 ratio. Each dot represents an individual organoid (NDC: n = 8–10, AD: n = 6–8).

(F and F′) Representative western blots of APP C-terminal fragment C99 detection (F) evaluated by APP-specific antibody (clone B-4). (F′) Quantification of western blot. β-Actin was used as a loading control. For each protein, 3 independent analyses were performed.

(G and G′) Representative western blots of Tau phosphorylation (G) evaluated by a panel of total Tau and four P-Tau antibodies. MAP2 (neuronal marker) and β-actin (loading control). (G′) Quantification of western blot. For each protein, 3–5 independent analyses were performed. P-Tau values were normalized to total Tau.

(H) Quantification of neurofilament-light (*NEFL*), -medium (*NEFM*), and -heavy (*NEFH*) chains using qPCR. Each dot represents a pooled sample of 5–9 COs (NDC: n = 6, AD: n = 6).

(I and I′) Representative western blots of NF detection (I) evaluated by NF-L-specific antibody. (I′) Quantification of western blot. β-Actin was used as a loading control. For each protein, 3 independent analyses were performed.

(J and J′) Representative western blots (J) of stress/apoptosis (p53, C-PARP) and senescence ($p16^{INK4a}$) markers and quantification normalized to β-actin (J′). For each marker, 3–5 independent analyses were performed, and each dot represents one analysis. β-Actin was used as a loading control.

(K and L) Treatment of AD-COs by β- and γ-secretase inhibitors. (K) Experimental layout. (L) Quantification of Aβ40 and Aβ42 peptides secreted into media (measured by ELISA) after treatment with inhibitors or DMSO (solvent control). Dots represent individual AD#2-COs (DMSO: n = 8–9; inhibitors: n = 9–10). *p < 0.05; **p < 0.01; ***p < 0.001. Error bars represent SEM.

See also Figure S2 and Table S1.

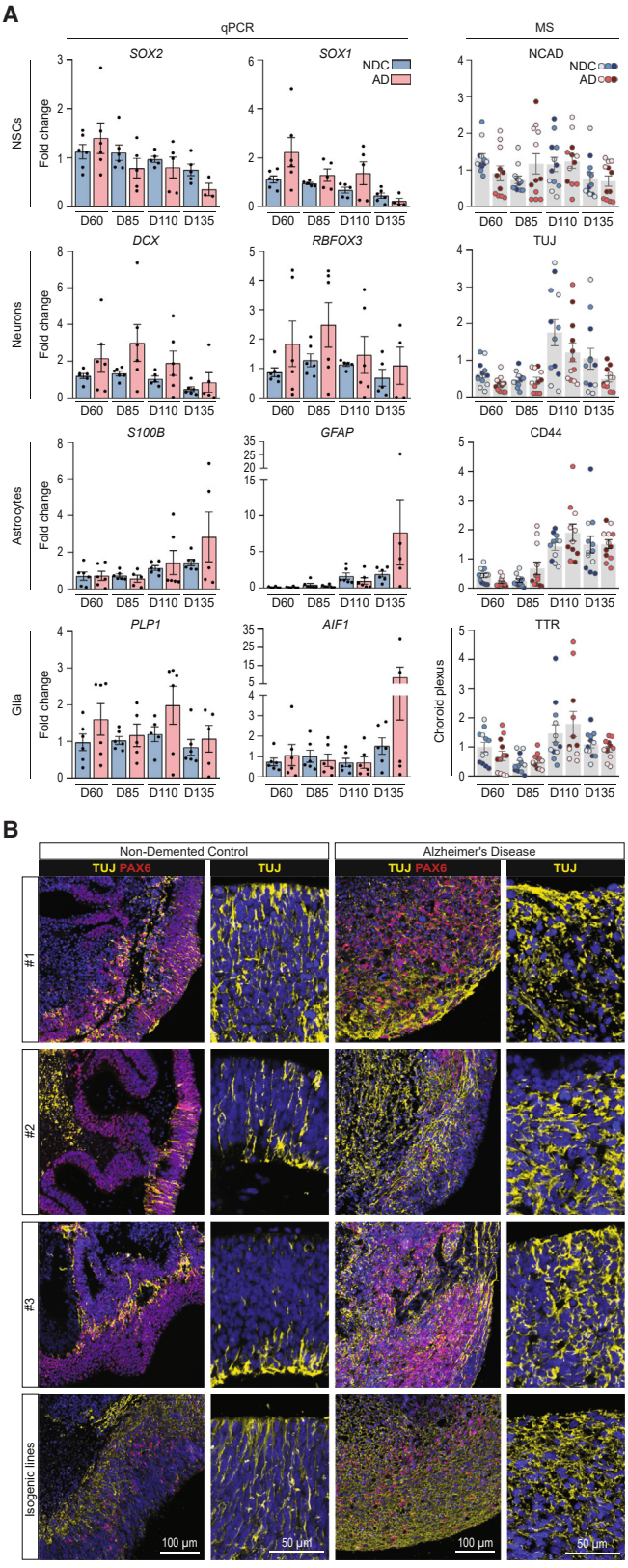

Figure 3. AD-iPSC-derived organoids show tissue patterning defects

(A) Quantification of mRNA (qPCR) and protein (MS) levels of cell-type-specific markers during CO differentiation. Neural stem cell (NSC) markers (qPCR: *SOX2*, *SOX1*; MS: NCAD), neuronal markers (qPCR: *DCX*, *RBFOX3*; MS: TUJ), astrocytic markers (qPCR: *S100B*, *GFAP*; MS: CD44), oligo-/microglial markers (qPCR: *PLP1* for oligodendrocytes, *AIF1* for microglia), and choroid plexus marker (MS: TTR). Each dot in the qPCR graphs represents a pooled sample of 5–9 COs (NDC: n = 6, AD: n = 6). Color-coded dots in MS graphs represent single organoids (NDC: n = 12, AD: n = 12). Error bars represent SEM.

(B) Representative images of COs (day 60) derived from three NDC- and three AD-iPSCs and a pair of isogenic i3N-iPSCs carrying *PSEN1*(A246E) mutation and respective wild-type control. Tissue organization on immunofluorescent staining of paraffin sections (scale bars: 100 µm) is depicted with neuronal (TUJ) and NSC (PAX6) markers. A magnified view of tissue organization is shown with TUJ staining only.

See also Figure S3 and Table S1.

Importantly, we validated the major findings using genetically identical, isogenic cell lines by employing a fourth independent wild-type iPSC line (i3N-iPSCs[21]) and introducing the *PSEN1*(A246E) mutation via CRISPR-Cas9 (Figure S2D). Our results demonstrate that, during the differentiation of i3N-iPSCs into COs, those carrying the *PSEN1*(A246E) mutation exhibited a significantly increased Aβ42/40 ratio and elevated levels of total APP compared with the wild-type COs at the two examined time points (days 60 and 95; Figures S2E, S2F, and S2F′). Furthermore, we observed increased expression of P-Tau on Ser202/Thr205 residues and a tendency toward upregulation of NF-L, C-PARP, and $p16^{INK4A}$ (Figures S2G and S2G′). These findings from the isogenic cell line thus corroborate the results obtained from iPSCs derived from patients, providing robust evidence that the AD-related markers are indeed induced by the PSEN mutation.

Lastly, we tested if the treatment of AD-COs by β- and γ-secretase inhibitors could ameliorate Aβ40 and Aβ42 secretion. We used COs derived from AD-iPSCs (day 50) and treated them simultaneously with β- and γ-secretase inhibitors for 25 and 50 days (Figure 2K). Analysis of secreted Aβ at both time points showed significantly downregulated levels of both Aβ40 and Aβ42 (Figure 2L). Thus, data confirmed that our AD-iPSC-derived COs gradually develop AD-related markers and are responsive to drug treatment.

AD-iPSC-derived organoids show tissue patterning defects

We subsequently compared the differentiation potential of AD- and NDC-COs. We first analyzed the differences in the gene expression of differentiation-associated markers during the previously selected four time points using qPCR and targeted MS analyses. Data (Figure 3A) showed that NDC- and AD-COs follow similar gene/protein expression patterns during their development *in vitro*. The initially highest expression of NSC markers (*SOX2*, *SOX1*, NCAD) at day 60 was followed by a peak in the expression of neuronal markers (*DCX*, *RBFOX3*, TUJ) at days 85–110. Markers specific for astrocytes (*S100B*, *GFAP*, CD44), oligodendrocytes (*PLP1*), microglia (*AIF1*/IBA1), and choroid plexus (TTR) only reached the peak of their expression during

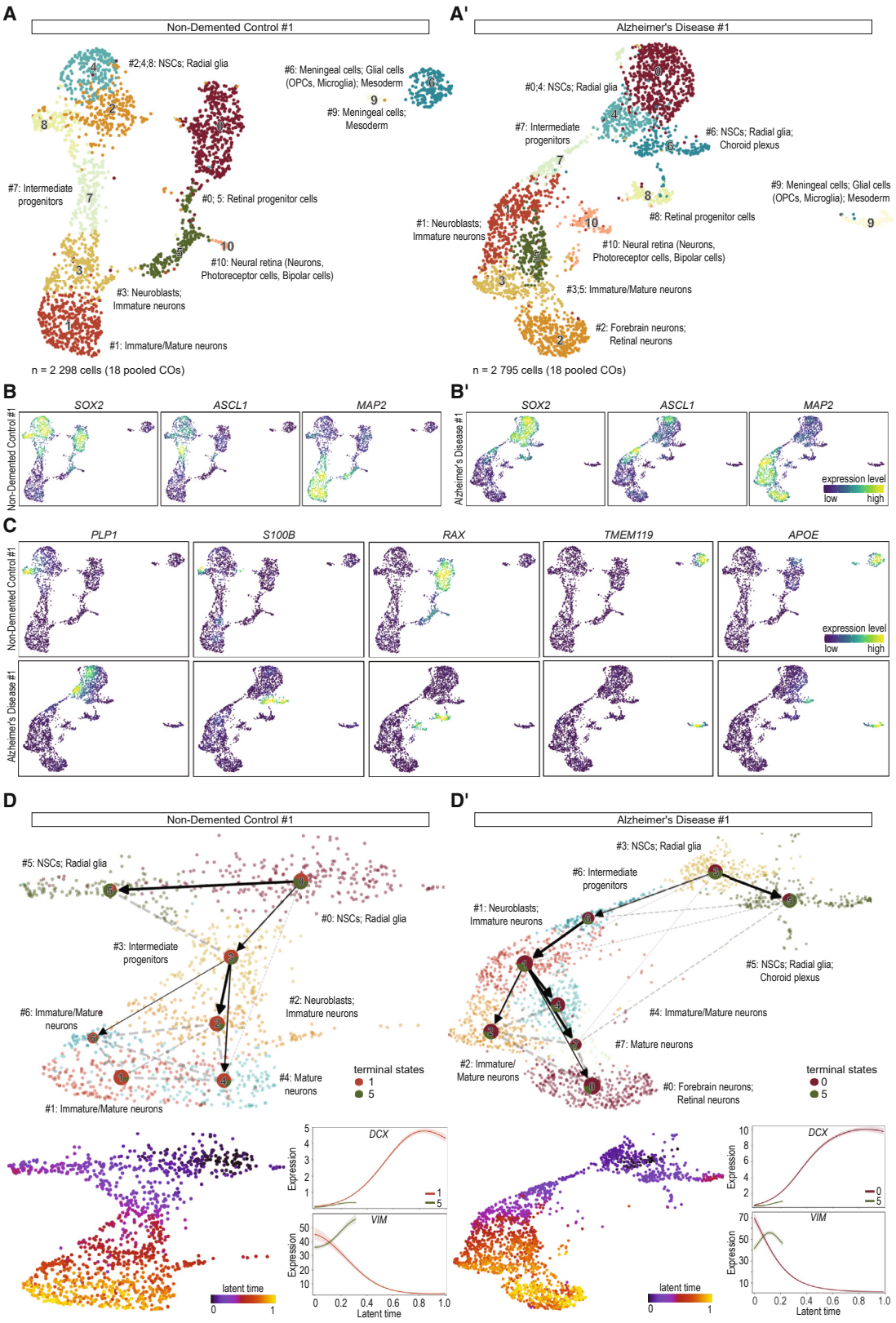

(legend on next page)

the last two collected time points (days 110 and 135). Although we noticed a trend in AD-COs toward a higher expression of neuronal genes, based on the overall expression dynamics, we concluded that both NDC- and AD-COs follow the typical human neurodevelopmental scheme, i.e., the appearance of NSCs and neurons is only later followed by the differentiation of glia and other non-neuronal cell types.

Subsequently, we performed immunohistochemistry (IHC) analysis to confirm the expression of selected markers and noticed striking differences in the tissue patterning. While COs derived from all three NDC-iPSC lines, as well as from the control i3N iPSCs, established the typical organoid patterning and tissue organization, AD-COs failed to correctly develop such a complex pattern, irrespective of the cell line used (Figure S3). As shown in Figure S3, only a minority of organoids possessing small areas of patterned clusters (marked by yellow arrow) could be found in analyzed cohorts of AD-COs. Specific staining for PAX6 and TUJ confirmed the lack of patterning and clearly showed that, compared with NDC-COs, AD-COs rarely developed layers of organized neuroepithelia (with polarized TUJ signal) and instead showed a highly disorganized pattern of the selected markers throughout the organoid (Figure 3B). Importantly, these phenotypical changes and lack of patterning were also found in COs derived from the isogenic iPSCs with introduced *PSEN1*(A246E) mutation (Figures S3 and 3B).

Single-cell RNA sequencing depicts the heterogeneity of NDC- and AD-iPSC-derived organoids

Prompted by the dissimilarities in the tissue organization between NDC- and AD-COs, we reasoned that this apparent heterogeneity would be underlain by distinct cell-type-specific gene expression. We thus performed single-cell RNA sequencing (scRNA-seq) of 60-day-old COs derived from AD#1-iPSCs, carrying a *PSEN1*(A246E) mutation and an *APOE3/3* genotype, and from this patient's age-, sex- and *APOE*-status-matched complementary healthy control subject (NDC#1). To compensate for the heterogeneity of organoids, 18 COs per sample were pooled, dissociated into single cells, and analyzed using the 10× Genomics platform. scRNA-seq reads underwent preprocessing, quality control, and filtering as described in the STAR Methods and resulted in retaining 2,298 and 2,795 cells per each NDC#1 and AD#1 sample, respectively.

First, we performed clustering of the individual scRNA-seq samples (i.e., without integrating the datasets), revealing 11 distinct populations in both NDC#1 and AD#1 samples (Figures 4A and 4A′). Clusters were then manually annotated based on cluster marker analysis, known markers, and the PanglaoDB database[22] (Figures S4A and S4A′). Expression of cell-type-specific markers for NSCs (*SOX2*, *SOX1*, *PAX6*), immature and mature neurons (*ASCL1*, *MAP2*, *NEUROD4*, *DCX*, *MAPT*), glia (*PLP1*, *S100B*, *TMEM119*), neural retina (*RAX*, *SIX3*), and *APOE* verified the presence of all these cell types in our day 60 CO populations, confirming our qPCR/MS data (Figures 4B, 4B′, 4C, and S4B). We then conducted the CellRank analysis (Figures 4D and 4D′), which combines trajectory inference with RNA velocity (Figures S4C and S4C′). The analysis revealed two similar developmental trajectories for both NDC#1- and AD#1-COs: one leading from the progenitor population toward mature neurons (marked, e.g., by the expression of the *DCX* gene; Figure 4D) and the second one leading from the progenitor population toward glial cell types (marked, e.g., by the expression of the *VIM* gene; Figure 4D′).

Markedly, this initial analysis of non-integrated datasets pointed out an intriguing observation: AD#1-COs contained a population of neurons absent from NDC#1-COs (Figure 4A′, cluster #2). Besides specifically expressing mature and immature neuronal markers, including *MAP2*, *MAPT*, *DCX*, and numerous others (Figure S4A′), we noticed that this population also expressed *PAX6* and *SIX3* (Figure S4B). These two markers represent crucial transcription factors with the ability to induce ectopic "mini eyes" in various tissues in lower vertebrates[23,24] and are also expressed in olfactory bulb neurons, where they regulate survival.[25,26] Our subsequent qPCR analysis from all our iPSC lines did not identify differences in the *PAX6* expression in AD-iPSC-derived COs compared with NDCs (Figure S4D), suggesting that the expression of *PAX6* and *SIX3* could represent altered development of part of the neuronal subpopulation. This hypothesis is supported by RNA velocity analysis, which identified a reversed "direction" of development in this specific cluster (Figure S4C′, here labeled as cluster #0: forebrain neurons; retinal neurons).

Integrated scRNA-seq data analysis confirms the altered developmental phenotype and signs of premature onset of differentiation in a subset of neurons

Finally, to directly probe the differences between AD- and NDC-COs, we integrated the datasets, performed clustering, and manually annotated the clusters described above (Figures 5A and S5A). To evaluate the success of the integration, we

Figure 4. Single-cell sequencing depicts the heterogeneity of NDC#1- and AD#1-iPSC-derived organoids

(A and A′) Uniform manifold approximation and projection (UMAP) plots of scRNA-seq data from a pooled sample of 18 organoids (day 60) derived from NDC#1-iPSC line (A; 2,298 cells) or AD#1-iPSC line (A′; 2,795 cells).

(B and B′) Expression of selected markers of NSCs (*SOX2*), intermediate progenitors/immature neurons (*ASCL1*), and mature neurons (*MAP2*) projected onto UMAP plots of scRNA-seq data from NDC#1-COs (B) or AD#1-COs (B′).

(C) Expression of selected markers of glia (oligodendrocytes: *PLP1*, astrocytes: *S100B*, microglia: *TMEM119*), retinal progenitor cells (*RAX*), and *APOE* expression projected onto UMAP plots of scRNA-seq data from NDC#1-COs (top) or AD#1-COs (bottom).

(D and D′) Differentiation trajectory analysis of neuronal lineage cells from NDC#1-COs (D) and AD#1-COs (D′). Top: PAGA plot of differentiation trajectories inferred by CellRank projected onto UMAP plot of scRNA-seq data. Clusters are shown as numbered pie charts, with colors representing average CellRank fate probabilities for progression to terminal states. Bottom left: latent time calculated with CellRank for trajectory inference. Bottom right: expression level over latent time for selected genes (*DCX*, *VIM*) along trajectories leading to terminal states predicted by CellRank. NSCs/radial glia, retinal progenitor cells, and neural retina cells were not included in this analysis.

See also Figure S4 and Table S1.

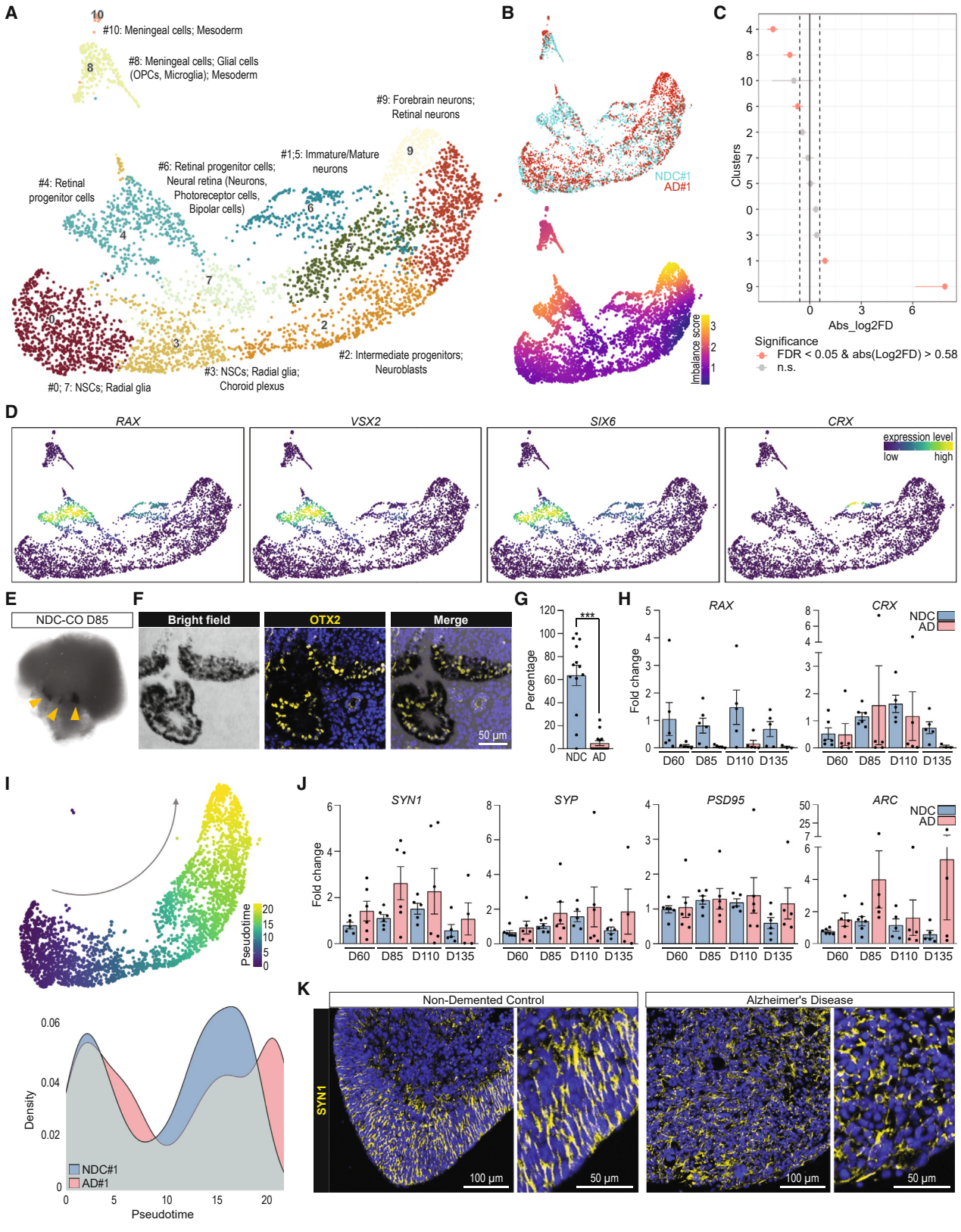

(legend on next page)

calculated and visualized the imbalance between the distributions of sample labels (Figure 5B). Despite the substantial overlap of both samples implying successful integration, there were clusters enriched for cells belonging to NDC#1 or AD#1 cell populations. To statistically validate the observed differences, we performed a permutation test for proportions (Figure 5C). The test identified cluster #4 as the most significantly enriched for cells from NDC#1-COs, whereas clusters #1 and #9 were identified as significantly enriched for cells from AD#1-COs. Our further analyses thus focused on these clusters and aimed to uncover the possible biological significance for their specific enrichment or absence in AD#1-iPSC-derived COs.

We initiated our analysis with cluster #4 enriched in the NDC#1 population, composed of retinal progenitor cells expressing markers such as *RAX*, *VSX2*, and *SIX6* (Figure 5D). The expression of *CRX*, a gene that plays a role in the differentiation of photoreceptor cells, was only detected in cluster #6, corresponding to a more mature neural retina (Figure 5D). This cell population of retinal progenitors (cluster #4) is likely required to generate the neural retina and retinal pigment epithelium, observable as the pigmented areas on mature organoids. Thus, we hypothesized that such a substantial absence of a cell population in AD#1-COs might result in a morphological phenotype—the absence of these pigmented areas on organoids. As they are easily visible during various stages of organoid development (Figure 5E), we first confirmed that they are indeed related to eye development. IHC analysis validated the co-localization of pigmented areas with orthodenticle homeobox 2 [OTX2], a critical protein in eye development[27] (Figure 5F). We then calculated the percentage of these pigmented areas on each organoid from various differentiation batches from all our six iPSC lines. Results confirmed that more than 60% of COs derived from NDC-iPSCs in each batch (n = 13) of differentiation contained at least one pigmented area. On the contrary, 14 evaluated batches of AD-COs contained these pigmented areas only rarely (~7%; Figure 5G). Analysis of *RAX* and *CRX* expression using qPCR also confirmed this phenotype, with both genes expressed more prominently in NDC-COs compared with AD-COs, irrespective of the cell line used (Figure 5H). As a comparison to *PSEN1/2* mutant iPSC-derived COs, we evaluated the percentage of pigmented areas on an isogenic pair of iPSCs carrying the London *APP* mutation (V717I) (Figure S5B, see the figure legend for more information). As shown in Figures S5C and S5D, *APP*(V717I)-iPSC-derived COs show the presence of AD-specific markers (increased Aβ42/40 ratio of secreted amyloids), but the percentage of organoids with pigmented areas remains similar to its isogenic control cell line. Taken together, our data from all six iPSC lines confirmed that, in comparison to NDC-iPSCs, AD-iPSC-derived COs failed to adequately initiate the development of retinal progenitor cells, which is later followed by the absence of pigmented OTX2+ epithelium on the surface of organoids. Data also suggest that the observed phenotype is more prominent in AD-COs with *PSEN1* and *PSEN2* mutations than with the (London) mutation in *APP*. Whether AD-COs carrying this APP mutation also exhibit developmental alterations remains to be investigated.

Finally, the integrated scRNA-seq analysis showed that cells in clusters #1 and #9 (corresponding to clusters #2 and #3 in non-integrated analysis, Figure 4A′) are either enriched in or almost exclusively from the AD#1-COs. Based on enriched genes in these clusters, cells were identified as having Mature neuronal identity (Figures 5A and S5A). At the same time, cluster #9 also expressed *PAX6* and *SIX3* genes, eye development and olfactory bulb neuron-related transcription factors (Figure S5A). Thus, to further explore differences in neuronal development between the conditions, we performed a pseudotime analysis. This analysis indicated that cluster #9, followed by cluster #1, is the most mature population from our dataset (Figure 5I). The top plot visualizes CO development from progenitors to neurons (marked by arrow). The bottom plot then clarifies that cells from AD#1-COs are more mature than those from NDC#1-COs. Interestingly, a comparison of our data with the Organoid Single-Cell Genomic Atlas[28] supported this observation and showed faster maturation of AD#1-COs (Figure S5E). Additionally, our qPCR data of selected neuronal and synaptic plasticity genes (*DCX*, *RBFOX3*/NeuN, *SYN1*, *SYP*, *PSD95*, *ARC*; Figures 3A and 5J) also point to the trend of increased expression in AD-COs, irrespective of the iPSC line used, suggesting a tendency in which more neurons are present in AD-COs. Lastly, when we performed IHC of the selected neuronal markers TUJ (Figure 3B) and SYN1 (Figure 5K), we noticed that their

Figure 5. Integrated data analysis confirms the altered developmental phenotype and signs of premature onset of differentiation in a subset of neurons

(A and B) UMAP plot of scRNA-seq dataset integrated from NDC#1-CO and AD#1-CO sequencing data. (A) Cluster annotation.

(B) Cells are color-coded according to sample origin (NDC#1, blue; AD#1, red; top) or by imbalance score (bottom).

(C) Point-range plot of permutation test results for individual clusters of the integrated dataset.

(D) Expression of selected markers of retinal progenitor (*RAX*, *VSX2*, *SIX6*) and photoreceptors (*CRX*).

(E) Representative picture of CO (day 85) with pigmented areas marked by the yellow arrow.

(F) Co-localization of pigmented areas (bright-field image) and fluorescently labeled marker of retinal development OTX2 on organoid (day 85) section.

(G) Percentage of organoids per differentiation batch with at least one dark spot. 268 NDC-COs (across 13 batches) and 182 AD COs (across 14 batches) were evaluated. Dots in the graph represent individual batches of differentiation (***$p < 0.001$).

(H) qPCR analyses of early eye development (*RAX*) and photoreceptor (*CRX*) markers during CO differentiation. Each dot represents the expression in 5–9 pooled COs (NDC: n = 6, AD: n = 6).

(I) Top: pseudotime inferred by Slingshot projected onto UMAP plot of the integrated scRNA-seq dataset. Bottom: cell density over pseudotime calculated for the integrated dataset. Cell densities are plotted individually for cells originating from NDC#1-COs (blue) or AD#1-COs (red).

(J) qPCR analyses of synaptic genes (*SYN1*, *SYP*, *PSD95*) and synaptic plasticity gene (*ARC*) during CO differentiation. Each dot represents a pooled sample of 5–9 COs (NDC: n = 6, AD: n = 6).

(K) Representative images of immunofluorescent staining of NDC- and AD-CO (day 60) paraffin sections with synapsin-1 (SYN1).

Error bars represent SEM.

See also Figure S5 and Table S1.

expression within organoids significantly differs. In AD-iPSC-derived COs, their expression pattern was visibly disorganized and distributed throughout the whole organoid compared to NDC-iPSC-derived organoids that showed an organized expression of TUJ and SYN1 in layers, suggesting that increased gene expression (and possibly faster differentiation) could be related to the failure of AD-COs to organize.

It has been previously suggested that premature differentiation of neurons in fAD-iPSC-based models could be attributed to *PSEN1* mutations leading to defective Notch signaling.[11,29,30] We thus further examined this hypothesis. Firstly, we used our scRNA-seq data to visualize Notch signaling effector genes (*HES1*, *HES4*, and *HES5*) (Figure S5F) and confirmed that they are all expressed in different progenitor clusters, with *HES1* being specifically highly expressed in populations enriched in retinal progenitor cells. Secondly, *HES1* and *HES4* expression revealed that, compared with NDC#1, they are downregulated in AD#1-COs and, based on dot plot visualization, also in most progenitor clusters (Figure S5G). Thirdly, qPCR analysis confirms that *HES1* expression is prominently downregulated in AD-COs derived from all three iPSC lines (Figure S5H). The last evidence of compromised Notch activity is the expression of *FABP7*/BLBP—a Notch readout gene specifically expressed in radial glia.[31] Both gene and protein expression showed a trend toward downregulated expression in AD-COs (Figures S5I and S5I′). All these data indicate that Notch signaling might indeed be altered in AD-iPSC-derived COs, likely from the beginning of CO differentiation, but the direct molecular link remains to be shown.

DISCUSSION

This study demonstrates that COs derived from AD-iPSCs with *PSEN1*(A246E) and *PSEN2*(N141I) mutations develop the AD-specific markers *in vitro*, yet it also uncovers tissue patterning defects and altered development supported by scRNA-seq. In particular, our experiments first confirm that AD-iPSC-derived COs form diffuse- and compact-like Aβ aggregates that gradually increase in size as organoids age *in vitro*. This is in line with previous studies that confirm the ability of iPSC-derived 3D models to mimic the Aβ-plaque-like formation from iPSCs (1) with fAD-causing mutations,[12,32,33] (2) from patients with Down syndrome possessing three copies of the *APP* gene,[34] and 3) from sAD cases.[9,10,35,36] Our data also show that the total level of APP is increased in AD-COs, potentially suggesting varying degrees of neuronal content in the organoids. However, our data also show that the neuronal MAP2 signal declines with the age of organoids, as opposed to APP, which remains relatively stable. This observation suggests that the elevated APP levels may be driven by a mechanism other than changes in neuronal content. However, the specific underlying mechanism responsible for this APP increase requires further investigation and remains to be elucidated. Still, in line with the study of Raja et al.[12] on neural organoids differentiated from fAD-iPSCs, we also confirm that the observed gradual formation of aggregates is accompanied by an increased Aβ42/40 ratio of secreted Aβ, and their levels can be pharmacologically ameliorated using β- and γ-secretase inhibitors.

Additionally, COs derived from all three AD-iPSC lines show common trends toward developing other AD-related markers. These include (1) hyperphosphorylated Tau protein (Ser202/Thr205); (2) higher expression of NFs; (3) a trend toward lower expression of *CHAT*, a marker of cholinergic neurons; and (4) statistically significant signs of ongoing cellular stress/apoptosis and senescence. Notably, several previous studies demonstrated hyperphosphorylation of Tau species present in both fAD- and sAD-COs,[12,33,36,37] although different reports showed distinct P-Tau epitopes that undergo hyperphosphorylation. Our study compares four different P-Tau-specific sites, and data show that the most specific upregulation in AD-COs derived from patients, as well as from isogenic iPSCs, is phosphorylation on Ser202/Thr205 residues (as detected by AT8 antibody). It still remains to be seen if organoids also possess detergent-insoluble fractions of Tau species as previously described in the brains of patients with AD.[38]

Furthermore, our study also shows that accompanying AD-related markers are also mimicked in this model, including NFs, integral constituents of the neuron playing a major role in brain development, maintenance, and regeneration. Specifically, the NF-L represents a robust predictive biomarker of ongoing neurodegeneration in patients with AD.[2] Rodent models also confirm NF-L in blood, and CSF can be used as a marker of disease progression.[39,40] And while most of the studies focus on secreted NF-L, there is evidence that NF-L accumulates, or is abnormally distributed, in AD brains. In particular, abnormal accumulation of variably phosphorylated NFs was associated with early cytoskeletal alterations and dystrophic neurite formation in AD.[41] Studies also reported abnormal distribution of NF-L in AD neurons and increased NF immunoreactivity in the hippocampus of patients with AD, with some neurons displaying "abnormal" sprouting processes.[42,43] Additionally, several publications consistently found NFs in senile plaques, tangles, and Lewy bodies in patients with AD.[44–50] Moreover, a study by Espuny-Camacho et al.[51] shows an abnormal accumulation of NFs in human neurons exposed to mouse Aβ in a chimeric human/mouse AD model, and Bajo et al.[52] show that different brain regions express different levels of NFs in patients with AD or Down syndrome and suggest an impaired structural assembly of NFs behind the observed phenomenon. Our study now shows that fAD-COs derived from three iPSC lines with *PSEN1*/*PSEN2* mutations exhibit a trend toward a higher expression of NF-L (as well as NF-M) and that their gene and protein expression increases with aging *in vitro.* Notably, the expression level of NF-L/NF-M in AD-COs differs from that of MAP2, which is downregulated with the aging of COs, suggesting that increased neuronal population or premature neuronal differentiation likely does not contribute to increased levels of NFs in our model. Lastly, our AD-COs also exhibit a trend toward a gradual decrease in the expression of the cholinergic neuron marker *CHAT*. It is known that cholinergic neurons in the basal forebrain are severely depleted in patients with AD.[3] Rodent models also support this finding,[53] and, indeed, several cholinesterase inhibitors are among the only two types of medication currently used to treat the symptoms of AD in human patients (reviewed in Ferreira-Vieira et al.[3]). Importantly, recent studies on human iPSC-based models have shown that stem cell-derived basal

forebrain cholinergic neurons from patients with AD have reduced excitability and impaired insulin-induced Ca^{2+} influx[54,55] and are more susceptible to cell death.[56] Our model now shows that the expression of *CHAT* (but not other neuronal markers) shows a trend toward lower expression in AD-COs compared with NDCs.

Finally, our fAD-CO model also clearly showed significantly upregulated markers of ongoing cellular stress/apoptosis (p53, C-PARP) and senescence ($p16^{INK4a}$). All these proteins have been previously associated with AD in both human and animal models (reviewed in Abate et al.[4]). iPSC-based 2D neuronal models of AD thus far confirm elevated apoptotic cell death and DNA-damage response pathway activation in neurons with fAD (*PSEN1*) mutations[30,57] as well as models from patients with sAD.[56] Our model now adds to these findings by showing extensive upregulation of cellular stress/apoptosis and senescence-related markers in 3D COs.

Importantly, our data bring novel evidence that despite similar expression of cell-type-specific genes and proteins during CO maturation *in vitro*, AD-COs derived from four independent iPSC lines show limited tissue patterning and altered cellular development. Since the complex neural diversity in the CNS is generated from a pool of neural progenitors that produce distinct cell types in a specific order, it is plausible that alteration in spatial patterning (spatial position of the progenitor) or temporal patterning (changing intrinsic and extrinsic signals) could result in an observed phenotype.[58] Indeed, it has been previously suggested that AD could be a disorder of mechanisms underlying structural brain self-organization,[59] and the increasing data indicate that early changes in brain development contribute, in general, to the manifestation of neurodegenerative diseases (reviewed in Faravelli et al.[13]). Several reports have then shown that patients with genetic risk of AD have functional and structural brain changes[60,61] or altered adult hippocampal neurogenesis.[62–64] Indeed, a growing number of reports suggest that, specifically, adult hippocampal neurogenesis drops sharply during the early stages of AD via unknown mechanisms and correlates with cognitive status in patients with AD (reviewed in Salta et al.[64]). Significantly, studies from iPSC-based models began to confirm that the differentiation potential of AD-derived NSCs or neurons might be compromised. However, it is still unclear what exactly underlies these changes. Several reports have brought evidence that AD-derived NSCs[29,30,35] and COs[11] likely prematurely differentiate. On the contrary, a few recently published studies report either the inability of neurons to adequately mature[65] or a neuronal de-differentiation.[66] All these reports have used different model systems and analytical methods, and it is thus challenging to draw a clear conclusion. Interestingly, our study, complemented by single-cell analysis, shows that both scenarios are not mutually exclusive, as we see a faster maturation of AD#1-iPSC-derived organoids. And since the AD-COs show limited tissue patterning, it is plausible that the inadequate spatial or temporal patterning early in the AD organoid differentiation inadequately stimulates neural progenitor pool development. This leads not only to premature differentiation of neurons but also to the lower diversity in cell populations, such as retinal progenitors. Future studies focused on sequencing early differentiation of AD-COs could provide valuable insights into the broader dynamics of the tissue development, as described previously for healthy human COs.[67]

Molecular mechanisms behind these phenomena, however, remain to be investigated. It has been proposed that progenitor populations in fAD-iPSC-derived neurons/COs with mutations in γ-secretase subunits might have compromised Notch signaling[68] and, therefore, prematurely differentiate.[11,29] Our data also suggest that Notch signaling molecules might play a role in AD, but the direct evidence and mechanism are currently missing. Moreover, PSEN1 and PSEN2 have evolutionarily conserved functions outside the γ-secretase complex: they play a role in regulating Wnt/β-catenin signaling, protein trafficking and degradation, calcium homeostasis, and apoptosis.[69] It is possible that any of these processes directly affect the ability of neural progenitors to timely specify the developmental fate and diversity of developing COs. However, this remains to be precisely determined in the future.

Limitations of the study

Our study has several limitations attributed to the inherent heterogeneity of the CO model. Even though some recent studies showed progress toward generating more uniform organoids *in vitro*,[70,71] it remains clear that this self-organizing system will always generate heterogeneous batches of organoids. We aimed to compensate for this "intrabatch" variability by pooling 5–9 organoids into one sample and for "interbatch" variability by performing at least 6 independent replicate experiments from three different cell lines for AD/NDC groups. We thus believe that, although some presented data do not show statistical significance, observed changes do represent the underlying biology of AD-specific markers. Another limitation is the small sample size (two cell lines) for scRNA-seq, which we aimed to partially compensate for by pooling 18 organoids per cell line into the analysis. Still, as we were aware of this constraint, we used stringent conditions/methods for data processing and, most importantly, reported on data that we could confirm on all three NDC- and three AD-COs. We also do not specifically refer to cluster #9, a subpopulation of mature neurons present only in the AD#1-CO sample set, as this result could be affected by the propensity of the AD#1 cell line used for the differentiation. Any future scRNA-seq analysis using a bigger sample size will surely provide not only insight into observed altered development but could also investigate morphogen/organizer differences in the scRNA-seq datasets and developmental patterning in AD and point toward specific genes that might be altered during the initiation of AD. Provided that repeated scRNA-seq would confirm the AD-enriched population of neurons, existing datasets could be screened to pinpoint neurons displaying a correlated signature. This could then be cross-referenced with other data outputs, like the occurrence of Aβ plaques in corresponding histological records.

STAR★METHODS

Detailed methods are provided in the online version of this paper and include the following:

- KEY RESOURCES TABLE

SUPPLEMENTAL INFORMATION

Supplemental information can be found online at https://doi.org/10.1016/j.celrep.2023.113310.

ACKNOWLEDGMENTS

The authors would like to thank Andrea Pacesova and Dagmar Bezdekova for sharing P-Tau antibodies; Gabriela Dovrtelova for help with optimization of MS sample preparation; Martin Barak for initiating the CO cultures in the lab; Jan Masek for helpful discussion on Notch signaling and for sharing the reagents; Lukas Cajanek and Tomas Barta for critical reading of the manuscript and discussion on retinal development; and Ales Hampl for his support. I3N-iPSCs were generously provided by M. Ward.[21] Funding for this research was provided by the Czech Science Foundation (21-21510S and 20-15728S [D.B.]); by the Czech Health Research Council - AZV (NU22-04-00366 [H.H.], NU22J-08-00075 [J.R.], NU21-08-00373 [D.B.], NU20-08-00314 [K.P.], and NV19-08-00472 [Z.S. and D.B.]); by the Grant Agency of Masaryk University (MUNI/A/1301/2022, and MUNI/G/1131/2017 [Z.S. and D.B.]); by the project "SORLA-FIX" (8F20009 [D.B.]) funded by MEYS CR/JPND; by the European Regional Development Fund - Project INBIO (CZ.02.1.01/0.0/0.0/16_026/0008451); and by RVO (65269705 [K.P.]) provided by the Ministry of Health of the Czech Republic. D.B., K.A.C., and T.V. were supported by funds from Alzheimer NF and Career Restart Grants (MUNI/R/1697/2020 and MUNI/R/1321/2021). V.F. and S.K. were supported by JCMM – PhD Talent and MUNI/IGA/1273/2021. Lastly, we also acknowledge Research Infrastructure RECETOX RI (LM2018121 and CZ.02.1.01/0.0/0.0/16_013/0001761), the core facility CELLIM supported by the Czech-BioImaging large RI project (LM2018129), and CF Genomics, supported by the NCLG research infrastructure (LM2018132), the European Union's Horizon 2020 research and innovation programme under grant agreement no. 857560, and the National Program of Sustainability II (no. LQ1605), all funded by the MEYS CR. We thank Operational Programme Research, Development and Innovation - project CETOCOEN EXCELLENCE (no. CZ.02.1.01/0.0/0.0/17_043/0009632) and CETOCOEN Plus (CZ.02.1.01/0.0/0.0/15_003/0000469) for their support with obtaining the scientific data presented in this paper. Researchers were also supported by project nos. LX22NPO5107 and ADDIT-CE 101087124 (MEYS), financed by the European Union. This publication reflects only the authors' views, and the European Commission is not responsible for any use that may be made of the information it contains.

AUTHOR CONTRIBUTIONS

T.V. and D.B. designed the project and wrote the manuscript with input from all authors. T.V., J.S., J.R., K.A.C., V.P., S.K., and M.N. performed experiments and collected and analyzed the data. P.T. performed bioinformatic analysis. V.F., H.K., M.C., P.O., P.F., S.B., and H.H. contributed reagents and technical expertise. K.P. and Z.S. helped with data interpretation. D.B., K.P., and Z.S. acquired funding. All authors read and agreed on the manuscript.

DECLARATION OF INTERESTS

The authors declare no competing interests.

INCLUSION AND DIVERSITY

We support inclusive, diverse, and equitable conduct of research.

Received: March 28, 2022
Revised: August 9, 2023
Accepted: October 4, 2023

REFERENCES

1. Dawkins, E., and Small, D.H. (2014). Insights into the physiological function of the β-amyloid precursor protein: beyond Alzheimer's disease. J. Neurochem. *129*, 756–769. https://doi.org/10.1111/jnc.12675.
2. Zetterberg, H., Skillbäck, T., Mattsson, N., Trojanowski, J.Q., Portelius, E., Shaw, L.M., Weiner, M.W., and Blennow, K.; Alzheimer's Disease Neuroimaging Initiative (2016). Association of Cerebrospinal Fluid Neurofilament Light Concentration With Alzheimer Disease Progression. JAMA Neurol. *73*, 60–67. https://doi.org/10.1001/jamaneurol.2015.3037.
3. Ferreira-Vieira, T.H., Guimaraes, I.M., Silva, F.R., and Ribeiro, F.M. (2016). Alzheimer's Disease: Targeting the Cholinergic System. Curr. Neuropharmacol. *14*, 101–115. https://doi.org/10.2174/1570159X13666150716165726.
4. Abate, G., Frisoni, G.B., Bourdon, J.-C., Piccirella, S., Memo, M., and Uberti, D. (2020). The pleiotropic role of p53 in functional/dysfunctional neurons: focus on pathogenesis and diagnosis of Alzheimer's disease. Alzheimer's Res. Ther. *12*, 160. https://doi.org/10.1186/s13195-020-00732-0.
5. Bhat, R., Crowe, E.P., Bitto, A., Moh, M., Katsetos, C.D., Garcia, F.U., Johnson, F.B., Trojanowski, J.Q., Sell, C., and Torres, C. (2012). Astrocyte Senescence as a Component of Alzheimer's Disease. PLoS One *7*, e45069. https://doi.org/10.1371/journal.pone.0045069.
6. De Strooper, B., and Karran, E. (2016). The Cellular Phase of Alzheimer's Disease. Cell *164*, 603–615. https://doi.org/10.1016/j.cell.2015.12.056.
7. Avior, Y., Sagi, I., and Benvenisty, N. (2016). Pluripotent stem cells in disease modelling and drug discovery. Nat. Rev. Mol. Cell Biol. *17*, 170–182. https://doi.org/10.1038/nrm.2015.27.
8. Barak, M., Fedorova, V., Pospisilova, V., Raska, J., Vochyanova, S., Sedmik, J., Hribkova, H., Klimova, H., Vanova, T., and Bohaciakova, D. (2022). Human iPSC-Derived Neural Models for Studying Alzheimer's Disease: from Neural Stem Cells to Cerebral Organoids. Stem Cell Rev. Rep. *18*, 792–820. https://doi.org/10.1007/s12015-021-10254-3.
9. Lin, Y.-T., Seo, J., Gao, F., Feldman, H.M., Wen, H.-L., Penney, J., Cam, H.P., Gjoneska, E., Raja, W.K., Cheng, J., et al. (2018). APOE4 Causes Widespread Molecular and Cellular Alterations Associated with

Alzheimer's Disease Phenotypes in Human iPSC-Derived Brain Cell Types. Neuron *98*, 1141–1154.e7. https://doi.org/10.1016/j.neuron.2018.05.008.

10. Zhao, J., Fu, Y., Yamazaki, Y., Ren, Y., Davis, M.D., Liu, C.-C., Lu, W., Wang, X., Chen, K., Cherukuri, Y., et al. (2020). APOE4 exacerbates synapse loss and neurodegeneration in Alzheimer's disease patient iPSC-derived cerebral organoids. Nat. Commun. *11*, 5540. https://doi.org/10.1038/s41467-020-19264-0.
11. Arber, C., Lovejoy, C., Harris, L., Willumsen, N., Alatza, A., Casey, J.M., Lines, G., Kerins, C., Mueller, A.K., Zetterberg, H., et al. (2021). Familial Alzheimer's Disease Mutations in PSEN1 Lead to Premature Human Stem Cell Neurogenesis. Cell Rep. *34*, 108615. https://doi.org/10.1016/j.celrep.2020.108615.
12. Raja, W.K., Mungenast, A.E., Lin, Y.-T., Ko, T., Abdurrob, F., Seo, J., and Tsai, L.-H. (2016). Self-Organizing 3D Human Neural Tissue Derived from Induced Pluripotent Stem Cells Recapitulate Alzheimer's Disease Phenotypes. PLoS One *11*, e0161969. https://doi.org/10.1371/journal.pone.0161969.
13. Faravelli, I., Costamagna, G., Tamanini, S., and Corti, S. (2020). Back to the origins: Human brain organoids to investigate neurodegeneration. Brain Res. *1727*, 146561. https://doi.org/10.1016/j.brainres.2019.146561.
14. Sherrington, R., Rogaev, E.I., Liang, Y., Rogaeva, E.A., Levesque, G., Ikeda, M., Chi, H., Lin, C., Li, G., Holman, K., et al. (1995). Cloning of a gene bearing missense mutations in early-onset familial Alzheimer's disease. Nature *375*, 754–760. https://doi.org/10.1038/375754a0.
15. Levy-Lahad, E., Wasco, W., Poorkaj, P., Romano, D.M., Oshima, J., Pettingell, W.H., Yu, C.E., Jondro, P.D., Schmidt, S.D., and Wang, K. (1995). Candidate gene for the chromosome 1 familial Alzheimer's disease locus. Science *269*, 973–977. https://doi.org/10.1126/science.7638622.
16. Rogaev, E.I., Sherrington, R., Rogaeva, E.A., Levesque, G., Ikeda, M., Liang, Y., Chi, H., Lin, C., Holman, K., and Tsuda, T. (1995). Familial Alzheimer's disease in kindreds with missense mutations in a gene on chromosome 1 related to the Alzheimer's disease type 3 gene. Nature *376*, 775–778. https://doi.org/10.1038/376775a0.
17. Raska, J., Hribkova, H., Klimova, H., Fedorova, V., Barak, M., Barta, T., Pospisilova, V., Vochyanova, S., Vanova, T., and Bohaciakova, D. (2021). Generation of six human iPSC lines from patients with a familial Alzheimer's disease (n = 3) and sex- and age-matched healthy controls (n = 3). Stem Cell Res. *53*, 102379. https://doi.org/10.1016/j.scr.2021.102379.
18. Lancaster, M.A., Renner, M., Martin, C.-A., Wenzel, D., Bicknell, L.S., Hurles, M.E., Homfray, T., Penninger, J.M., Jackson, A.P., and Knoblich, J.A. (2013). Cerebral organoids model human brain development and microcephaly. Nature *501*, 373–379. https://doi.org/10.1038/nature12517.
19. Röhr, D., Boon, B.D.C., Schuler, M., Kremer, K., Hoozemans, J.J.M., Bouwman, F.H., El-Mashtoly, S.F., Nabers, A., Großerueschkamp, F., Rozemuller, A.J.M., and Gerwert, K. (2020). Label-free vibrational imaging of different Aβ plaque types in Alzheimer's disease reveals sequential events in plaque development. Acta Neuropathol. Commun. *8*, 222. https://doi.org/10.1186/s40478-020-01091-5.
20. Pulina, M.V., Hopkins, M., Haroutunian, V., Greengard, P., and Bustos, V. (2020). C99 selectively accumulates in vulnerable neurons in Alzheimer's disease. Alzheimers Dement. *16*, 273–282. https://doi.org/10.1016/j.jalz.2019.09.002.
21. Fernandopulle, M.S., Prestil, R., Grunseich, C., Wang, C., Gan, L., and Ward, M.E. (2018). Transcription Factor–Mediated Differentiation of Human iPSCs into Neurons. Curr. Protoc. Cell Biol. *79*, e51. https://doi.org/10.1002/cpcb.51.
22. Franzén, O., Gan, L.-M., and Björkegren, J.L.M. (2019). PanglaoDB: a web server for exploration of mouse and human single-cell RNA sequencing data. Database 2019, baz046.. https://doi.org/10.1093/database/baz046
23. Sasai, Y., Eiraku, M., and Suga, H. (2012). In vitro organogenesis in three dimensions: self-organising stem cells. Development *139*, 4111–4121. https://doi.org/10.1242/dev.079590.
24. Liu, W., Lagutin, O.V., Mende, M., Streit, A., and Oliver, G. (2006). Six3 activation of Pax6 expression is essential for mammalian lens induction and specification. EMBO J. *25*, 5383–5395. https://doi.org/10.1038/sj.emboj.7601398.
25. Ninkovic, J., Pinto, L., Petricca, S., Lepier, A., Sun, J., Rieger, M.A., Schroeder, T., Cvekl, A., Favor, J., and Götz, M. (2010). The Transcription Factor Pax6 Regulates Survival of Dopaminergic Olfactory Bulb Neurons via Crystallin αA. Neuron *68*, 682–694. https://doi.org/10.1016/j.neuron.2010.09.030.
26. Conte, I., Morcillo, J., and Bovolenta, P. (2005). Comparative analysis of Six3 and Six6 distribution in the developing and adult mouse brain. Dev. Dynam. *234*, 718–725. https://doi.org/10.1002/dvdy.20463.
27. Martinez-Morales, J.R., Signore, M., Acampora, D., Simeone, A., and Bovolenta, P. (2001). Otx genes are required for tissue specification in the developing eye. Development *128*, 2019–2030.
28. Kanton, S., Boyle, M.J., He, Z., Santel, M., Weigert, A., Sanchís-Calleja, F., Guijarro, P., Sidow, L., Fleck, J.S., Han, D., et al. (2019). Organoid single-cell genomic atlas uncovers human-specific features of brain development. Nature *574*, 418–422. https://doi.org/10.1038/s41586-019-1654-9.
29. Koch, P., Tamboli, I.Y., Mertens, J., Wunderlich, P., Ladewig, J., Stüber, K., Esselmann, H., Wiltfang, J., Brüstle, O., and Walter, J. (2012). Presenilin-1 L166P Mutant Human Pluripotent Stem Cell–Derived Neurons Exhibit Partial Loss of γ-Secretase Activity in Endogenous Amyloid-β Generation. Am. J. Pathol. *180*, 2404–2416. https://doi.org/10.1016/j.ajpath.2012.02.012.
30. Yang, J., Zhao, H., Ma, Y., Shi, G., Song, J., Tang, Y., Li, S., Li, T., Liu, N., Tang, F., et al. (2017). Early pathogenic event of Alzheimer's disease documented in iPSCs from patients with PSEN1 mutations. Oncotarget *8*, 7900–7913. https://doi.org/10.18632/oncotarget.13776.
31. Anthony, T.E., Mason, H.A., Gridley, T., Fishell, G., and Heintz, N. (2005). Brain lipid-binding protein is a direct target of Notch signaling in radial glial cells. Genes Dev. *19*, 1028–1033. https://doi.org/10.1101/gad.1302105.
32. Ghatak, S., Dolatabadi, N., Trudler, D., Zhang, X., Wu, Y., Mohata, M., Ambasudhan, R., Talantova, M., and Lipton, S.A. (2019). Mechanisms of hyperexcitability in Alzheimer's disease hiPSC-derived neurons and cerebral organoids vs isogenic controls. Elife *8*, e50333. https://doi.org/10.7554/eLife.50333.
33. Gonzales, K.A.U., Liang, H., Lim, Y.-S., Chan, Y.-S., Yeo, J.-C., Tan, C.-P., Gao, B., Le, B., Tan, Z.-Y., Low, K.-Y., et al. (2015). Deterministic Restriction on Pluripotent State Dissolution by Cell-Cycle Pathways. Cell *162*, 564–579. https://doi.org/10.1016/j.cell.2015.07.001.
34. Alić, I., Goh, P.A., Murray, A., Portelius, E., Gkanatsiou, E., Gough, G., Mok, K.Y., Koschut, D., Brunmeir, R., Yeap, Y.J., et al. (2020). Patient-specific Alzheimer-like pathology in trisomy 21 cerebral organoids reveals BACE2 as a gene dose-sensitive AD suppressor in human brain. Mol. Psychiatr., 1–23. https://doi.org/10.1038/s41380-020-0806-5.
35. Meyer, K., Feldman, H.M., Lu, T., Drake, D., Lim, E.T., Ling, K.-H., Bishop, N.A., Pan, Y., Seo, J., Lin, Y.-T., et al. (2019). REST and Neural Gene Network Dysregulation in iPSC Models of Alzheimer's Disease. Cell Rep. *26*, 1112–1127.e9. https://doi.org/10.1016/j.celrep.2019.01.023.
36. Park, J.-C., Jang, S.-Y., Lee, D., Lee, J., Kang, U., Chang, H., Kim, H.J., Han, S.-H., Seo, J., Choi, M., et al. (2021). A logical network-based drug-screening platform for Alzheimer's disease representing pathological features of human brain organoids. Nat. Commun. *12*, 280. https://doi.org/10.1038/s41467-020-20440-5.
37. Hernández, D., Rooney, L.A., Daniszewski, M., Gulluyan, L., Liang, H.H., Cook, A.L., Hewitt, A.W., and Pébay, A. (2021). Culture Variabilities of Human iPSC-Derived Cerebral Organoids Are a Major Issue for the Modelling of Phenotypes Observed in Alzheimer's Disease. Stem Cell Rev and Rep. https://doi.org/10.1007/s12015-021-10147-5.
38. Mukherjee, S., Dubois, C., Perez, K., Varghese, S., Birchall, I.E., Leckey, M., Davydova, N., McLean, C., Nisbet, R.M., Roberts, B.R., et al. (2023). Quantitative proteomics of tau and Aβ in detergent fractions from

Alzheimer's disease brains. J. Neurochem. *164*, 529–552. https://doi.org/10.1111/jnc.15713.

39. Bacioglu, M., Maia, L.F., Preische, O., Schelle, J., Apel, A., Kaeser, S.A., Schweighauser, M., Eninger, T., Lambert, M., Pilotto, A., et al. (2016). Neurofilament Light Chain in Blood and CSF as Marker of Disease Progression in Mouse Models and in Neurodegenerative Diseases. Neuron *91*, 56–66. https://doi.org/10.1016/j.neuron.2016.05.018.

40. Qin, T., Prins, S., Groeneveld, G.J., Van Westen, G., de Vries, H.E., Wong, Y.C., Bischoff, L.J.M., and de Lange, E.C.M. (2020). Utility of Animal Models to Understand Human Alzheimer's Disease, Using the Mastermind Research Approach to Avoid Unnecessary Further Sacrifices of Animals. Int. J. Mol. Sci. *21*, 3158. https://doi.org/10.3390/ijms21093158.

41. Dickson, T.C., King, C.E., McCormack, G.H., and Vickers, J.C. (1999). Neurochemical diversity of dystrophic neurites in the early and late stages of Alzheimer's disease. Exp. Neurol. *156*, 100–110. https://doi.org/10.1006/exnr.1998.7010.

42. Nakamura, Y., Hasimoto, R., Kashiwagi, Y., Miyamae, Y., Shinosaki, K., Nishikawa, T., Hattori, H., Kudo, T., and Takeda, M. (1997). Abnormal distribution of neurofilament L in neurons with Alzheimer's disease. Neurosci. Lett. *225*, 201–204. https://doi.org/10.1016/s0304-3940(97)00223-1.

43. Vickers, J.C., Riederer, B.M., Marugg, R.A., Buée-Scherrer, V., Buée, L., Delacourte, A., and Morrison, J.H. (1994). Alterations in neurofilament protein immunoreactivity in human hippocampal neurons related to normal aging and Alzheimer's disease. Neuroscience *62*, 1–13. https://doi.org/10.1016/0306-4522(94)90310-7.

44. Cras, P., Kawai, M., Lowery, D., Gonzalez-DeWhitt, P., Greenberg, B., and Perry, G. (1991). Senile plaque neurites in Alzheimer disease accumulate amyloid precursor protein. Proc. Natl. Acad. Sci. USA *88*, 7552–7556. https://doi.org/10.1073/pnas.88.17.7552.

45. Schmidt, M.L., Lee, V.M., and Trojanowski, J.Q. (1991). Comparative epitope analysis of neuronal cytoskeletal proteins in Alzheimer's disease senile plaque neurites and neuropil threads. Lab. Invest. *64*, 352–357.

46. Su, J.H., Cummings, B.J., and Cotman, C.W. (1996). Plaque biogenesis in brain aging and Alzheimer's disease. I. Progressive changes in phosphorylation states of paired helical filaments and neurofilaments. Brain Res. *739*, 79–87. https://doi.org/10.1016/s0006-8993(96)00811-6.

47. Zhang, H., Sternberger, N.H., Rubinstein, L.J., Herman, M.M., Binder, L.I., and Sternberger, L.A. (1989). Abnormal processing of multiple proteins in Alzheimer disease. Proc. Natl. Acad. Sci. USA *86*, 8045–8049. https://doi.org/10.1073/pnas.86.20.8045.

48. Doering, L.C. (1993). Probing modifications of the neuronal cytoskeleton. Mol. Neurobiol. *7*, 265–291. https://doi.org/10.1007/BF02769179.

49. Trojanowski, J.Q., Schmidt, M.L., Shin, R.W., Bramblett, G.T., Rao, D., and Lee, V.M. (1993). Altered tau and neurofilament proteins in neurodegenerative diseases: diagnostic implications for Alzheimer's disease and Lewy body dementias. Brain Pathol. *3*, 45–54. https://doi.org/10.1111/j.1750-3639.1993.tb00725.x.

50. Pollanen, M.S., Bergeron, C., and Weyer, L. (1994). Characterization of a shared epitope in cortical Lewy body fibrils and Alzheimer paired helical filaments. Acta Neuropathol. *88*, 1–6. https://doi.org/10.1007/BF00294352.

51. Espuny-Camacho, I., Arranz, A.M., Fiers, M., Snellinx, A., Ando, K., Munck, S., Bonnefont, J., Lambot, L., Corthout, N., Omodho, L., et al. (2017). Hallmarks of Alzheimer's Disease in Stem-Cell-Derived Human Neurons Transplanted into Mouse Brain. Neuron *93*, 1066–1081.e8. https://doi.org/10.1016/j.neuron.2017.02.001.

52. Bajo, M., Yoo, B.C., Cairns, N., Gratzer, M., and Lubec, G. (2001). Neurofilament proteins NF-L, NF-M and NF-H in brain of patients with Down syndrome and Alzheimer's disease. Amino Acids *21*, 293–301. https://doi.org/10.1007/s007260170015.

53. Shekari, A., and Fahnestock, M. (2021). Chapter 13 - Cholinergic neurodegeneration in Alzheimer disease mouse models. In Handbook of Clinical Neurology the Human Hypothalamus: Neuropsychiatric Disorders, D.F. Swaab, R.M. Buijs, F. Kreier, P.J. Lucassen, and A. Salehi, eds. (Elsevier), pp. 191–209. https://doi.org/10.1016/B978-0-12-819973-2.00013-7.

54. Moreno, C.L., Della Guardia, L., Shnyder, V., Ortiz-Virumbrales, M., Kruglikov, I., Zhang, B., Schadt, E.E., Tanzi, R.E., Noggle, S., Buettner, C., and Gandy, S. (2018). iPSC-derived familial Alzheimer's PSEN2N141I cholinergic neurons exhibit mutation-dependent molecular pathology corrected by insulin signaling. Mol. Neurodegener. *13*, 33. https://doi.org/10.1186/s13024-018-0265-5.

55. Ortiz-Virumbrales, M., Moreno, C.L., Kruglikov, I., Marazuela, P., Sproul, A., Jacob, S., Zimmer, M., Paull, D., Zhang, B., Schadt, E.E., et al. (2017). CRISPR/Cas9-Correctable mutation-related molecular and physiological phenotypes in iPSC-derived Alzheimer's PSEN2N141Ineurons. Acta Neuropathol. Commun. *5*, 77. https://doi.org/10.1186/s40478-017-0475-z.

56. Duan, L., Bhattacharyya, B.J., Belmadani, A., Pan, L., Miller, R.J., and Kessler, J.A. (2014). Stem cell derived basal forebrain cholinergic neurons from Alzheimer's disease patients are more susceptible to cell death. Mol. Neurodegener. *9*, 3. https://doi.org/10.1186/1750-1326-9-3.

57. Wezyk, M., Szybinska, A., Wojsiat, J., Szczerba, M., Day, K., Ronnholm, H., Kele, M., Berdynski, M., Peplonska, B., Fichna, J.P., et al. (2018). Overactive BRCA1 Affects Presenilin 1 in Induced Pluripotent Stem Cell-Derived Neurons in Alzheimer's Disease. J. Alzheimers Dis. *62*, 175–202. https://doi.org/10.3233/JAD-170830.

58. Kohwi, M., and Doe, C.Q. (2013). Temporal fate specification and neural progenitor competence during development. Nat. Rev. Neurosci. *14*, 823–838. https://doi.org/10.1038/nrn3618.

59. Arendt, T. (2001). Alzheimer's disease as a disorder of mechanisms underlying structural brain self-organization. Neuroscience *102*, 723–765. https://doi.org/10.1016/S0306-4522(00)00516-9.

60. Adriaanse, S.M., Binnewijzend, M.A.A., Ossenkoppele, R., Tijms, B.M., van der Flier, W.M., Koene, T., Smits, L.L., Wink, A.M., Scheltens, P., van Berckel, B.N.M., and Barkhof, F. (2014). Widespread Disruption of Functional Brain Organization in Early-Onset Alzheimer's Disease. PLoS One *9*, e102995. https://doi.org/10.1371/journal.pone.0102995.

61. Quiroz, Y.T., Schultz, A.P., Chen, K., Protas, H.D., Brickhouse, M., Fleisher, A.S., Langbaum, J.B., Thiyyagura, P., Fagan, A.M., Shah, A.R., et al. (2015). Brain Imaging and Blood Biomarker Abnormalities in Children With Autosomal Dominant Alzheimer Disease: A Cross-Sectional Study. JAMA Neurol. *72*, 912–919. https://doi.org/10.1001/jamaneurol.2015.1099.

62. Terreros-Roncal, J., Moreno-Jiménez, E.P., Flor-García, M., Rodríguez-Moreno, C.B., Trinchero, M.F., Cafini, F., Rábano, A., and Llorens-Martín, M. (2021). Impact of neurodegenerative diseases on human adult hippocampal neurogenesis. Science *374*, 1106–1113. https://doi.org/10.1126/science.abl5163.

63. Toda, T., Parylak, S.L., Linker, S.B., and Gage, F.H. (2019). The role of adult hippocampal neurogenesis in brain health and disease. Mol. Psychiatr. *24*, 67–87. https://doi.org/10.1038/s41380-018-0036-2.

64. Salta, E., Lazarov, O., Fitzsimons, C.P., Tanzi, R., Lucassen, P.J., and Choi, S.H. (2023). Adult hippocampal neurogenesis in Alzheimer's disease: A roadmap to clinical relevance. Cell Stem Cell *30*, 120–136. https://doi.org/10.1016/j.stem.2023.01.002.

65. Mertens, J., Herdy, J.R., Traxler, L., Schafer, S.T., Schlachetzki, J.C.M., Böhnke, L., Reid, D.A., Lee, H., Zangwill, D., Fernandes, D.P., et al. (2021). Age-dependent instability of mature neuronal fate in induced neurons from Alzheimer's patients. Cell Stem Cell *28*, 1533–1548.e6. https://doi.org/10.1016/j.stem.2021.04.004.

66. Caldwell, A.B., Liu, Q., Schroth, G.P., Galasko, D.R., Yuan, S.H., Wagner, S.L., and Subramaniam, S. (2020). Dedifferentiation and neuronal repression define familial Alzheimer's disease. Sci. Adv. *6*, eaba5933. https://doi.org/10.1126/sciadv.aba5933.

67. Fleck, J.S., Jansen, S.M.J., Wollny, D., Zenk, F., Seimiya, M., Jain, A., Okamoto, R., Santel, M., He, Z., Camp, J.G., et al. (2023). Inferring and

perturbing cell fate regulomes in human brain organoids. Nature *621*, 365–372. https://doi.org/10.1038/s41586-022-05279-8.

68. Hurley, E.M., Mozolewski, P., Dobrowolski, R., and Hsieh, J. (2023). Familial Alzheimer's disease-associated PSEN1 mutations affect neurodevelopment through increased Notch signaling. Stem Cell Rep. *18*, 1516–1533. https://doi.org/10.1016/j.stemcr.2023.05.018.
69. Duggan, S.P., and McCarthy, J.V. (2016). Beyond gamma-secretase activity: The multifunctional nature of presenilins in cell signalling pathways. Cell. Signal. *28*, 1–11. https://doi.org/10.1016/j.cellsig.2015.10.006.
70. Chen, C., Rengarajan, V., Kjar, A., and Huang, Y. (2021). A matrigel-free method to generate matured human cerebral organoids using 3D-Printed microwell arrays. Bioact. Mater. *6*, 1130–1139. https://doi.org/10.1016/j.bioactmat.2020.10.003.
71. Sivitilli, A., Ghiasi, P., and Attisano, L. (2021). Production of Phenotypically Uniform Human Cerebral Organoids from Pluripotent Stem Cells. Bio. Protoc. *11*, e3985. https://doi.org/10.21769/BioProtoc.3985.
72. Bohaciakova, D., Renzova, T., Fedorova, V., Barak, M., Kunova Bosakova, M., Hampl, A., and Cajanek, L. (2017). An Efficient Method for Generation of Knockout Human Embryonic Stem Cells Using CRISPR/Cas9 System. Stem Cell. Dev. *26*, 1521–1527. https://doi.org/10.1089/scd.2017.0058.
73. Raska, J., Klimova, H., Sheardova, K., Fedorova, V., Hribkova, H., Pospisilova, V., Vochyanova, S., Vanova, T., and Bohaciakova, D. (2021). Generation of three human iPSC lines from patients with a spontaneous late-onset Alzheimer's disease and three sex- and age-matched healthy controls. Stem Cell Res. *53*, 102378. https://doi.org/10.1016/j.scr.2021.102378.
74. Kwart, D., Gregg, A., Scheckel, C., Murphy, E.A., Paquet, D., Duffield, M., Fak, J., Olsen, O., Darnell, R.B., and Tessier-Lavigne, M. (2019). A Large Panel of Isogenic APP and PSEN1 Mutant Human iPSC Neurons Reveals Shared Endosomal Abnormalities Mediated by APP β-CTFs, Not Aβ. Neuron *104*, 256–270.e5. https://doi.org/10.1016/j.neuron.2019.07.010.
75. Xie, Y., Wang, D., Lan, F., Wei, G., Ni, T., Chai, R., Liu, D., Hu, S., Li, M., Li, D., et al. (2017). An episomal vector-based CRISPR/Cas9 system for highly efficient gene knockout in human pluripotent stem cells. Sci. Rep. *7*, 2320. https://doi.org/10.1038/s41598-017-02456-y.
76. Lancaster, M.A., and Knoblich, J.A. (2014). Generation of cerebral organoids from human pluripotent stem cells. Nat. Protoc. *9*, 2329–2340. https://doi.org/10.1038/nprot.2014.158.
77. Nezvedová, M., Jha, D., Váňová, T., Gadara, D., Klímová, H., Raška, J., Opálka, L., Bohačiaková, D., and Spáčil, Z. (2023). Single Cerebral Organoid Mass Spectrometry of Cell-Specific Protein and Glycosphingolipid Traits. Anal. Chem. *95*, 3160–3167. https://doi.org/10.1021/acs.analchem.2c00981.
78. Fedorova, V., Pospisilova, V., Vanova, T., Amruz Cerna, K., Abaffy, P., Sedmik, J., Raska, J., Vochyanova, S., Matusova, Z., Houserova, J., et al. (2023). Glioblastoma and cerebral organoids: development and analysis of an in vitro model for glioblastoma migration. Mol. Oncol. *17*, 647–663. https://doi.org/10.1002/1878-0261.13389.
79. Fedorova, V., Vanova, T., Elrefae, L., Pospisil, J., Petrasova, M., Kolajova, V., Hudacova, Z., Baniariova, J., Barak, M., Peskova, L., et al. (2019). Differentiation of neural rosettes from human pluripotent stem cells in vitro is sequentially regulated on a molecular level and accomplished by the mechanism reminiscent of secondary neurulation. Stem Cell Res. *40*, 101563. https://doi.org/10.1016/j.scr.2019.101563.
80. Susaki, E.A., Tainaka, K., Perrin, D., Yukinaga, H., Kuno, A., and Ueda, H.R. (2015). Advanced CUBIC protocols for whole-brain and whole-body clearing and imaging. Nat. Protoc. *10*, 1709–1727. https://doi.org/10.1038/nprot.2015.085.
81. Schneider, C.A., Rasband, W.S., and Eliceiri, K.W. (2012). NIH Image to ImageJ: 25 years of image analysis. Nat. Methods *9*, 671–675. https://doi.org/10.1038/nmeth.2089.
82. Peskova, L., Jurcikova, D., Vanova, T., Krivanek, J., Capandova, M., Sramkova, Z., Sebestikova, J., Kolouskova, M., Kotasova, H., Streit, L., and Barta, T. (2020). miR-183/96/182 cluster is an important morphogenetic factor targeting PAX6 expression in differentiating human retinal organoids. Stem Cell. *38*, 1557–1567. https://doi.org/10.1002/stem.3272.
83. Vidova, V., Stuchlikova, E., Vrbova, M., Almasi, M., Klanova, J., Thon, V., and Spacil, Z. (2019). Multiplex Assay for Quantification of Acute Phase Proteins and Immunoglobulin A in Dried Blood Spots. J. Proteome Res. *18*, 380–391. https://doi.org/10.1021/acs.jproteome.8b00657.
84. Sucha, R., Kubickova, M., Cervenka, J., Hruska-Plochan, M., Bohaciakova, D., Vodickova Kepkova, K., Novakova, T., Budkova, K., Susor, A., Marsala, M., et al. (2021). Targeted mass spectrometry for monitoring of neural differentiation. Biol. Open *10*, bio058727. https://doi.org/10.1242/bio.058727.
85. Vidova, V., and Spacil, Z. (2017). A review on mass spectrometry-based quantitative proteomics: Targeted and data independent acquisition. Anal. Chim. Acta *964*, 7–23. https://doi.org/10.1016/j.aca.2017.01.059.
86. Butler, A., Hoffman, P., Smibert, P., Papalexi, E., and Satija, R. (2018). Integrating single-cell transcriptomic data across different conditions, technologies, and species. Nat. Biotechnol. *36*, 411–420. https://doi.org/10.1038/nbt.4096.
87. Young, M.D., and Behjati, S. (2020). SoupX removes ambient RNA contamination from droplet-based single-cell RNA sequencing data. GigaScience *9*, giaa151. https://doi.org/10.1093/gigascience/giaa151.
88. Alquicira-Hernandez, J., and Powell, J.E. (2021). Nebulosa recovers single-cell gene expression signals by kernel density estimation. Bioinformatics *37*, 2485–2487. https://doi.org/10.1093/bioinformatics/btab003.
89. Aran, D., Looney, A.P., Liu, L., Wu, E., Fong, V., Hsu, A., Chak, S., Naikawadi, R.P., Wolters, P.J., Abate, A.R., et al. (2019). Reference-based analysis of lung single-cell sequencing reveals a transitional profibrotic macrophage. Nat. Immunol. *20*, 163–172. https://doi.org/10.1038/s41590-018-0276-y.
90. Bray, N.L., Pimentel, H., Melsted, P., and Pachter, L. (2016). Near-optimal probabilistic RNA-seq quantification. Nat. Biotechnol. *34*, 525–527. https://doi.org/10.1038/nbt.3519.
91. Bergen, V., Lange, M., Peidli, S., Wolf, F.A., and Theis, F.J. (2020). Generalizing RNA velocity to transient cell states through dynamical modeling. Nat. Biotechnol. *38*, 1408–1414. https://doi.org/10.1038/s41587-020-0591-3.
92. Lange, M., Bergen, V., Klein, M., Setty, M., Reuter, B., Bakhti, M., Lickert, H., Ansari, M., Schniering, J., Schiller, H.B., et al. (2022). CellRank for directed single-cell fate mapping. Nat. Methods *19*, 159–170. https://doi.org/10.1038/s41592-021-01346-6.
93. Blischak, J.D., Carbonetto, P., and Stephens, M. (2019). Creating and Sharing Reproducible Research Code the Workflowr Way. https://doi.org/10.12688/f1000research.20843.1.
94. He, Z., Brazovskaja, A., Ebert, S., Camp, J.G., and Treutlein, B. (2020). CSS: cluster similarity spectrum integration of single-cell genomics data. Genome Biol. *21*, 224. https://doi.org/10.1186/s13059-020-02147-4.
95. Miller, S.A., Policastro, R.A., Sriramkumar, S., Lai, T., Huntington, T.D., Ladaika, C.A., Zentner, G.E., and O'Hagan, H.M. (2020). LSD1 Promotes Secretory Cell Specification to Drive BRAF Mutant Colorectal Cancer. https://doi.org/10.1101/2020.09.25.313536.
96. Street, K., Risso, D., Fletcher, R.B., Das, D., Ngai, J., Yosef, N., Purdom, E., and Dudoit, S. (2018). Slingshot: cell lineage and pseudotime inference for single-cell transcriptomics. BMC Genom. *19*, 477. https://doi.org/10.1186/s12864-018-4772-0.
97. Grubbs, F.E. (1969). Procedures for Detecting Outlying Observations in Samples. Technometrics *11*, 1–21. https://doi.org/10.1080/00401706.1969.10490657.

STAR★METHODS

KEY RESOURCES TABLE

REAGENT or RESOURCE	SOURCE	IDENTIFIER
Antibodies		
β-Actin (8H10D10); WB; 1:10,000 in 5% milk	Cell Signaling Technology	Cat# 3700; RRID: AB_2242334
p53 (DO-1); WB; 1:2,000 in 5% milk	generously provided by Bořivoj Vojtěšek, Masaryk Memorial Cancer Institute, Brno, Czech Republic	Clone DO-1 (Bohaciakova et al.)[72]
Cleaved PARP (Asp214) (D64E10); WB; 1:1,000 in 5% milk	Cell Signaling Technology	Cat# 5625; RRID: AB_10699459
$p16^{INK4a}$ (D7C1M); WB; 1:1,000 in 5% milk	Cell Signaling Technology	Cat# 80772; RRID: AB_2799960
MAP2 (D5G1); WB; 1:1,000 in 5% milk; IHC, 1:300	Cell Signaling Technology	Cat# 8707; RRID: AB_2722660
Tau (D-8); WB; 1:500 in 5% milk	Santa Cruz Biotechnology	Cat# sc-166060; RRID: AB_2266085
Phospho-Tau (Ser202, Thr205) (AT-8); WB; 1:1,500 in 5% BSA	Thermo Fisher Scientific	Cat# MN1020; RRID: AB_223647
Phospho-Tau (Thr231); WB; 1:4,000 in 5% BSA	Thermo Fisher Scientific	Cat# 44-746G; RRID: AB_2533742
Phospho-Tau (Ser356); WB; 1:500 in 5% BSA	Abcam	Cat# ab75603; RRID: AB_1310736
Phospho-Tau (Thr181); WB, 1:1000 in 5% BSA	Thermo Fisher Scientific	Cat# MN1050 RRID: AB_223651
beta-Amyloid (B-4); WB, 1:500 in 5% milk	Santa Cruz Biotechnology	Cat# sc-28365; RRID: AB_626669
GFAP (D1F4Q); IHC, 1:200; Whole-mount, 1:100	Cell Signaling Technology	Cat# 12389; RRID: AB_2631098
MAP2; IHC, 1:100; Whole-mount, 1:100	Merck	Cat# AB5543; RRID: AB_571049
TUJ (TU-20); IHC, 1:100	Cell Signaling Technology	Cat# 4466; RRID: AB_1904176
PAX6 (D3A9V); IHC, 1:100	Cell Signaling Technology	Cat# 60433; RRID: AB_2797599
SOX2 (L1D6A2); IHC, 1:100	Cell Signaling Technology	Cat# 4900; RRID: AB_10560516
SOX1; IHC, 1:100	Cell Signaling Technology	Cat# 4194; RRID: AB_1904140
TTR (FL-147); IHC, 1:100	Santa Cruz Biotechnology	Cat# sc-13098; RRID: AB_2241313
NCAD (D4R1H); IHC, 1:100	Cell Signaling Technology	Cat# 13116; RRID: AB_2687616
SATB2 (SATBA4B10); IHC, 1:100	Santa Cruz Biotechnology	Cat# sc-81376; RRID: AB_1129287
CTIP2 (D6F1); IHC, 1:100	Cell Signaling Technology	Cat# 12120; RRID: AB_2797823
DCX (E−6); IHC, 1:100	Santa Cruz Biotechnology	Cat# sc-271390; RRID: AB_10610966
NeuN (D4G4O); IHC, 1:100	Cell Signaling Technology	Cat# 2430; RRID: AB_2651140

(*Continued on next page*)

Continued

REAGENT or RESOURCE	SOURCE	IDENTIFIER
Synapsin-1 (D12G5); IHC, 1:200	Cell Signaling Technology	Cat# 5297; RRID: AB_2616578
NF-L (C28E10); IHC, 1:200; WB; 1:500 in 5% milk	Cell Signaling Technology	Cat# 2837; RRID: AB_823575
beta-Amyloid (D54D2); IHC, 1:100	Cell Signaling Technology	Cat# 8243; RRID: AB_2797642
OTX2 (D-8); IHC, 1:100	Santa Cruz Biotechnology	Cat# sc-514195; RRID: AB_291699
Anti-rabbit IgG, HRP-linked Antibody; WB, 1:3,000	Cell Signaling Technology	Cat# 7074; RRID: AB_2099233
Anti-Mouse IgG (whole molecule)-Peroxidase antibody produced in goat; WB, 1:3,000	Merck	Cat# A4416; RRID: AB_258167
Donkey anti-Rabbit IgG (H + L) Highly Cross-Adsorbed Secondary Antibody, Alexa Fluor 568; IHC, 1:250	Thermo Fisher Scientific	Cat# A10042; RRID: AB_2534017
Donkey anti-Mouse IgG (H + L) Highly Cross-Adsorbed Secondary Antibody, Alexa Fluor 488; IHC, 1:250	Thermo Fisher Scientific	Cat#A-21202; RRID: AB_141607
Alexa Fluor 647-AffiniPure Donkey Anti-Chicken IgY; IHC, 1:250	Jackson ImmunoResearch Labs	Cat# 703-605-155; RRID: AB_2340379
Chemicals, peptides, and recombinant proteins		
mTeSR™1	STEMCELL technologies	Cat# 85850
Matrigel® hESC-Qualified Matrix, LDEV-free	Corning	Cat# 354277
Zell Shield Cell Culture Contamination Preventive	Minerva Biolabs	Cat# 13-0050
EDTA (0.5 M), pH 8.0, RNase-free	Thermo Fisher Scientific	Cat# AM9260G
StemPro™ Accutase™ Cell Dissociation Reagent	Thermo Fisher Scientific	Cat# A1110501
DMEM/F12, no glutamine	Thermo Fisher Scientific	Cat# 21331046
Neurobasal ™ medium	Thermo Fisher Scientific	Cat# 21103049
N-2 Supplement (100X)	Thermo Fisher Scientific	Cat# 17502-048
B-27™ Supplement (50X), serum free	Thermo Fisher Scientific	Cat# 17504-044
B-27™ Supplement (50X), minus vitamin A	Thermo Fisher Scientific	Cat# 12587-010
GlutaMAX™ Supplement	Thermo Fisher Scientific	Cat# 35050061
MEM Non-Essential Amino Acids Solution (100X)	Thermo Fisher Scientific	Cat# 11140035
Heparin sodium salt from porcine intestinal mucosa	Merck	Cat# H3149
2-Mercaptoethanol	Merck	Cat# M3148
Insulin solution human	Merck	Cat# I9278
Y-27632 2HCL (ROCK inhibitor)	Selleckchem	Cat# S1049
Geltrex™ LDEV-Free, hESC-Qualified, Reduced Growth Factor Basement Membrane Matrix	Thermo Fisher Scientific	Cat# A1413301
poly(2-hydroxyethyl methacrylate) (poly-HEMA)	Merck	Cat# P3932
Dimethyl sulfoxide (DMSO)	Merck	Cat# D2650
β-Secretase Inhibitor IV - CAS 797035-11-1 - Calbiochem	Merck	Cat# 565788
γ-Secretase Inhibitor XXI, Compound E – CAS 209986-17-4 - Calbiochem	Merck	Cat# 565790
Essential 6™ Medium	Thermo Fisher Scientific	Cat# A1516401
Ammonium bicarbonate, BioUltra, ≥99.5% purity	Merck	Cat# 09830
Sodium deoxycholate, BioXtra, ≥98.0% purity	Merck	Cat# 30970
Iodoacetamide, ≥99%purity	Merck	Cat# I6125
1,4-dithiothreitol, ≥99%purity	Carl Roth GmbH+Co. KG	Cat# 6908.1
Acetonitrile, LC-MS grade	Honeywell	Cat# 34967
Isopropanol, LC-MS grade	Honeywell	Cat# 34965
Formic acid, for MS, ~98% purity	Honeywell	Cat# 94318

(*Continued on next page*)

Continued

REAGENT or RESOURCE	SOURCE	IDENTIFIER
Trypsin gold, Mass Spec Grade	Promega	Cat# V528A
Stable isotopically labeled peptide standards, customized synthesis	JPT Peptide Technologies Inc.	https://www.jpt.com/reference-peptides-for-targeted-proteomics-spiketides/7
eSpCas9-GFP Protein	Merck	Cat# ECAS9GFPPR-50UG
EpiCRISPR vector	Addgene (gift from Yongming Wang)	RRID: Addgene_135960
Lipofectamine™ Stem Transfection Reagent	Thermo Fisher Scientific	Cat# STEM00001
Opti-MEM™	Thermo Fisher Scientific	Cat# 31985062
FokI Restriction enzyme	New England Biolabs	Cat# R0109S
StyI-HF Restriction Enzyme	New England Biolabs	Cat# R3500S
BclI-HF Restriction Enzyme	New England Biolabs	Cat# R3160S
FBS	Thermo Fisher Scientific	Cat# 10270106
Collagenase P	Merck	Cat# 11213865001
HBSS	Merck	Cat# H8264
Goat serum	Merck	Cat# G9023
HOECHST 33342	Invitrogen	Cat# H1399
4′,6-diamidino-2-phenylindole (DAPI)	Carl Roth	Cat# R63351
RNA Blue	Top-Bio	Cat# R013
Critical commercial assays		
Amyloid beta 40 Human ELISA Kit	Thermo Fisher Scientific	Cat# KHB3481
Amyloid beta 42 Human ELISA Kit, Ultrasensitive	Thermo Fisher Scientific	Cat# KHB3544
Chromium Next GEM Single Cell 3' GEM, Library & Gel Bead Kit v3.1	10x Genomics	Cat# PN-1000121
Chromium Next GEM Chip G Single Cell Kit	10x Genomics	Cat# PN-1000120
Pierce BCA Protein Assay Kit	ThermoFisher Scientific	Cat# 23225
DC™ Protein Assay	Bio-Rad	Cat# 5000116
Transcriptor First Strand cDNA Synthesis Kit	Roche	Cat# 4897030001
LightCycler® 480 SYBR Green I Master kit	Roche	Cat# 4887352001
High Sensitivity NGS Fragment Analysis Kit	Agilent Technologies	Cat# DNF-474
NextSeq 500/550 High Output 75 Cycles Kit v2.5	Illumina	Cat# 20024906
Deposited data		
scRNA-seq: data	Annotare 2.0	ArrayExpress: E-MTAB-11438
scRNA-seq: reports with code	GitHub	GitHub: https://petrsh.github.io/AD_CO_scRNAseq
Files for interactive visualization with PAGODA	Mendeley Data	Mendeley Data: https://doi.org/10.17632/6r36skj6s6.1
Experimental models: Cell lines		
fAD1 hiPSC line (AD#1)	Raska et al.[17]	hPSCreg: #MUNIi005-A
fAD2 hiPSC line (AD#2)	Raska et al.[17]	hPSCreg: #MUNIi006-A
fAD3 hiPSC line (AD#3)	Raska et al.[17]	hPSCreg: #MUNIi007-A
fHC1 hiPSC line (NDC#1)	Raska et al.[17]	hPSCreg: #MUNIi008-A
fHC2 hiPSC line (NDC#2)	Raska et al.[17]	hPSCreg: #MUNIi009-A
fHC3 hiPSC line (NDC#3)	Raska et al.[17]	hPSCreg: #MUNIi010-A
fHC1 hiPSC line (NDC#1) *APP* V717I (London)	See Figure S5B for details	N/A
I3N hiPSC line (NDC)	generously provided by Dr. M. Ward, NIH	Fernandopulle et al.[21]
I3N hiPSC line *PSEN1* A246E	See Figure S2D for details	N/A
Oligonucleotides		
APP(London) CRISPR gRNA - UUUCUUCUUCA GCAUCACCA	Merck	N/A

(*Continued on next page*)

Continued

REAGENT or RESOURCE	SOURCE	IDENTIFIER
APP(London) CRISPR ssODN - TCATGGTGGG CGGTGTTGTCATAGCGACAGTGATCATCATC ACGTTGGTGATGCTGAAGAAGAAACAGT ACACATCCATT	Merck	N/A
APP(London) Forward primer - CATGGAAGC ACACTGATTCGT	Merck	N/A
APP(London) Reverse primer - CATCCAAA TGTCCCCTGCAT	Merck	N/A
PSEN1(A246E) CRISPR gRNA-ATGGACTGC GTGGCTCATCT	Merck	N/A
PSEN1(A246E) CRISPR ssODN – CATGGCCCTGGTGTTTATCAAGTACCTC CCTGAATGGACTGAGTGGCTC ATCCTAGCTGTGATTTCAGTATATG GTAAAACCCAAGACTGATAATTTGTT	Merck	N/A
PSEN1(A246E) Forward primer – TGGAATTTTGGTGTGGTGGGA	Merck	N/A
PSEN1(A246E) Reverse primer – GGGGCATTCCTGTGACAAAC	Merck	N/A
Primers for qPCR		See Table S2
Software and algorithms		
Skyline software	MacCoss Lab	version: 21.1.0.146
Adobe Illustrator	https://www.adobe.com/cz/products/illustrator.html	RRID:SCR_010279
ImageJ	https://imagej.net/	RRID:SCR_003070
ZEN Imaging Software	https://www.zeiss.com/microscopy/int/products/microscope-software/zen-lite.html	N/A
GraphPad Prism	https://www.graphpad.com/scientific-software/prism/	v8.0.1 RRID:SCR_002798
Biorender	https://biorender.com/	RRID:SCR_018361
Pagoda	https://github.com/kharchenkolab/pagoda2	v 1.0.4 RRID:SCR_01709
CellRanger	10x Genomics	v 5.0.1
Loompy	http://loompy.org/	v 3.0.0 RRID:SCR_016666
Kallisto	https://pachterlab.github.io/kallisto/	v 0.46.2 RRID:SCR_016582
scVelo	https://github.com/theislab/scvelo	v 0.2.3 RRID:SCR_018168
CellRank	https://github.com/theislab/cellrank	v 1.4.0
Seurat	https://github.com/satijalab/seurat	v 4.0.3 RRID:SCR_016341
Slingshot	https://github.com/kstreet13/slingshot	v 2.0.0 RRID:SCR_017012
SingleR	https://github.com/LTLA/SingleR	v 1.6.1
simspec	https://github.com/quadbiolab/simspec	N/A
scProportionTest	https://github.com/rpolicastro/scProportionTest	N/A
Nebulosa	https://github.com/powellgenomicslab/Nebulosa	v 1.2.0

(*Continued on next page*)

Continued

REAGENT or RESOURCE	SOURCE	IDENTIFIER
SoupX	https://github.com/constantAmateur/SoupX	v 1.5.2 RRID:SCR_019193
Other		
Agilent 1290 Infinity II LC System	Agilent Technologies	https://www.agilent.com/en/product/liquid-chromatography-mass-spectrometry-lc-ms
Agilent 6495B Triple Quadrupole LC/MS	Agilent Technologies	https://www.agilent.com/en/product/liquid-chromatography-mass-spectrometry-lc-ms
ACQUITY UPLC CSH 1.7 μm, 2.1 mm × 100 mm	Waters Corporation	https://www.waters.com/nextgen/us/en/shop/columns/186005297-acquity-uplc-csh-c18-column-130a-17–m-21-mm-x-100-mm-1-pk.html
NextSeq 500	Illumina	https://emea.illumina.com/systems/sequencing-platforms/nextseq.html
VEGA TS 5136 XM	Tescan Orsay	https://www.tescan.com/
Zeiss Axio Observer.Z1 with confocal unit LSM 800	Zeiss	https://www.zeiss.com/microscopy/int/products/confocal-microscopes.html
Zeiss Lightsheet 7	Zeiss	https://www.zeiss.com/microscopy/int/products/imaging-systems/light-sheet-microscope-for-lsfm-imaging-of-live-and-cleared-samples-lightsheet-7.html
TissueFaxs	TissueGnostic GmbH	https://tissuegnostics.com/products/fluorescence-cytometer/tissuefaxs-fluo
Neon™ Transfection System	Thermo Fisher Scientific	https://www.thermofisher.com/order/catalog/product/MPK5000

RESOURCE AVAILABILITY

Lead contact

Further information and requests for resources and reagents should be directed to and will be fulfilled by the lead contact, Dasa Bohaciakova (bohaciakova@med.muni.cz).

Materials availability

Cell lines generated in this study are available upon reasonable request and may require a completed materials transfer agreement.

Data and code availability

- Sequence data have been deposited in ArrayExpress: E-MTAB-11438. The reports with the computational code are available at GitHub: https://petrsh.github.io/AD_CO_scRNAseq. Files for interactive visualization with PAGODA can be downloaded from Mendeley Data: https://doi.org/10.17632/6r36skj6s6.1. PAGODA can be accessed using the following link: http://pklab.med.harvard.edu/nikolas/pagoda2/frontend/current/pagodaLocal/index.html
- This paper does not report original code.
- Any additional information required to reanalyze the data reported in this work paper is available from the lead contact upon request.

EXPERIMENTAL MODEL AND STUDY PARTICIPANT DETAILS

Cell culture of iPSCs

Three human patients-specific iPSC lines and three control iPSC lines were derived from individuals with fAD (here referred to as AD#1–3) and complementary (sex-, age-, and *APOE* status-matched) non-demented controls (here referred to as NDC#1–3; Listed in Figure S1A). They were passaged and maintained using standard feeder-free culture protocols as previously described in.[17,73] In brief, feeder-free cultures were grown on Matrigel-coated plates (Corning) in mTeSR1 (STEMCELL Technologies) and passaged

using 0.5 mM EDTA (Thermo Fisher Scientific) in PBS or manually. Used cell lines (listed in Key Resources table) were derived from fibroblasts deposited in Coriell Institute (Repository Reference ID numbers AG06840, AG06848, AG09908, GM23967, GM23251, GM03525), characterized,[17] and registered at Human Pluripotent Stem Cell Registry (hpscreg.eu).

Generation of the isogenic NDC#1 line with *APP* London (V717I) mutation using CRISPR/Cas9 knock-in

For the generation of the CRISPR/Cas9-mediated KI of London (V717I) mutation into the *APP* gene of NDC#1-iPSCs, a mixture of gRNA, Cas9-GFP protein, and ssODN was transfected into iPSCs using the Neon Transfection System (Thermo Fisher Scientific). Specifically, 1.2 μg of gRNA (Merck) was mixed with 3 μg Cas9-GFP protein (ECAS9GFPPR-50UG, Merck) and incubated for 10 min 150 pmol of ssODN (Merck) carrying the London mutation and an additional silent mutation to prevent re-cutting of DNA was added to the formed ribonucleoprotein (RNP) complex and transfected into 300,000 cells using the Neon Transfection system (1 pulse, 30 ms, 1,100 V; Thermo Fischer Scientific). The next day, cells were single-cell sorted into 96 well plates using FACS based on GFP signal. Single-cell clones were cultivated until colonies were formed. DNA was extracted from each clone using 100 μL of 100 mM NaOH (95°C, 20 min), followed by the addition of 100 μL 40 nM Tris-HCl (4°C, 1 h). Editing efficiency in each clone was analyzed by PCR followed by restriction enzyme digestion with BclII-HF and StyI-HF restriction enzymes (cutting edited and non-edited DNA, respectively; New England Biolabs) and visualized on 2% agarose gel. Clones identified as potentially edited were sequenced to validate the sequence of the mutated region. gRNA and ssODN sequences are listed in the Key Resources table.

Generation of the isogenic i3N cell line with *PSEN1* (A246E) mutation using CRISPR/Cas9 knock-in (KI)

For the generation of the CRISPR/Cas9-mediated KI of A246E mutation into the *PSEN1* gene of i3N-iPSCs, we cloned gRNA for *PSEN1* A246E mutation[74] into epiCRISPR plasmid.[75] Subsequently, epiCRISPR plasmid with cloned gRNA and ssODN was transfected into iPSCs using the Lipofectamine Stem Transfection Reagent (Thermo Fisher Scientific). Specifically, for vector preparation, gRNA was cloned into epiCRISPR vector according to the published protocol.[75] To generate the knock-in (KI), 2 μg of epiCRISPR vector (with cloned gRNA) and 6 μg ssODN for HDR (in 100 μL Opti-MEM; Thermo Fisher Scientific) was mixed with 7.5 μL Lipofectamine Stem Transfection Reagent (in 100 μL Opti-MEM) and incubated for 10 min. The transfection mix was incubated with 400,000 attached cells. After 48 h, cells were single-cell sorted into 96 well plates using FACS based on the GFP signal. Single-cell clones were cultivated until colonies were formed. DNA was extracted from each clone using 100 μL of 100 mM NaOH (95°C, 20 min), followed by the addition of 100 μL 40 mM Tris-HCl (4°C, 1 h). Individual clones were analyzed by PCR followed by restriction enzyme digestion with FokI restriction enzyme (cutting edited DNA; New England Biolabs) and visualized on 2% agarose gel. Selected clones were sequenced for confirmation (SeqMe). As a control (NDC), i3N-iPSCs that underwent the same process but without vectors were used. gRNA and ssODN sequences are listed in the Key Resources table.

Cerebral organoid culture and treatment with β- and γ-secretase inhibitors

COs were generated using the protocol described previously,[76–78] with few modifications. For the embryoid body (EB) formation from iPSCs, cells were detached by Accutase (Thermo Fisher Scientific) and plated at day 0 (D0) into non-adherent V-shaped 96-well plates at the density of 2,000–3,000 cells in mTeSR1 with 50 μM ROCK inhibitor (Selleckchem). Non-adherent cell culture plates were prepared with a coating of poly(2-hydroxyethyl methacrylate) (poly-HEMA; Merck). On D2, the medium was exchanged for the fresh mTeSR1 without ROCK inhibitor. When EBs reached the size of at least 400 μm, a fresh Neuroinduction medium[76] was added to EBs every day for 6 days (usually from D3 to D8). Subsequently, organoids were embedded in 7 μL of cold Geltrex (Thermo Fisher Scientific). Solidified Geltrex drops with organoids were gently detached and cultured without shaking in Cerebral Organoid Differentiation Medium [CODM;[76]] without vitamin A for 7 days. Subsequently, organoids were cultured in CODM with vitamin A and moved to an orbital shaker at D24-D28. ZellShield (Minerva Biolabs) was used for cell culture contamination prevention in all media. mTeSR1 was supplemented with only half of the recommended dose of ZellShield.

The treatment with β- and γ-secretase inhibitors was performed according to[12] on AD#2-COs for 25 and 50 days starting at D50. During the treatment, CODM was supplemented with 5 μM β-Secretase Inhibitor IV (Merck) and 6 nM γ-Secretase Inhibitor XXI (Compound E; Merck) freshly added on each day of the medium exchange. A respective amount of DMSO was added to control organoids as a solvent control.

METHOD DETAILS

Western blotting

Protein lysis and Western blotting were performed as described previously.[79] Briefly, protein samples of pooled organoids (approx. 5–9 COs) were lysed in 1% SDS-lysis buffer, the concentration was measured with DC Protein Assay (Bio-Rad) mixed with 10x Laemmli buffer and incubated at 95°C for 10 min. Proteins were separated on 10–15% Acrylamide gel and transferred onto PVDF membranes (Merck). Membranes were blocked and incubated with antibodies in 5% skimmed milk or BSA. Antibodies and specific conditions are listed in the key resource table. Densitometric analysis of Western blot scans was performed using ImageJ software and plotted as bar graphs with dots representing individual CO batches [each cell line (NDC/AD#1, #2, #3) was used at least once in all Western blot analyses].

RNA isolation, cDNA synthesis, qPCR

Total RNA from a sample (5–9 pooled COs) was isolated by RNA Blue reagent (Top-Bio) according to the manufacturer's instructions. The isolated RNA was transcribed to cDNA using Transcriptor First Strand cDNA Synthesis Kit (Roche) according to the manufacturer's instructions. qPCR was performed from the cDNA samples using LightCycler 480 SYBR Green I Master kit (Roche) on LightCycler 480 II (Roche). Ct values were calculated using the automated Second Derivative Maximum Method in LC480 software (Roche). Data were processed by calculating ΔCt ($Ct_{gene} - Ct_{housekeeping}$) and subsequently $2^{-\Delta Ct}$. The differentiation of NDC- and respective AD-COs were done simultaneously. Thus, the values were normalized to the average value of the respective NDC cell line. Dots in the graphs represent individual differentiation batches, and each cell line (NDC/AD#1, #2, #3) was used at least twice in all qPCR analyses. Specific primers are listed in Table S2.

Histological preparation of organoid samples, microscopy, and β-amyloid quantification

Before all immunostaining methods, harvested COs were fixed with 3.7% paraformaldehyde for 1 h.

Histological sections

ections were prepared on cryostat Leica 1850. Excessing O.C.T. medium was removed by a 15 min PBS wash prior to IHC staining. For paraffin sections, fixed COs were embedded in 3% agarose (Merck), followed by paraffin embedding. Paraffin blocks were cut into 2 μm thin sections that were further deparaffinized in xylene, rehydrated through a descending ethanol series (96-80-70-50% ethanol), and treated by antigen retrieval (pH6, DAKO) prior to IHC staining.

Immunohistochemistry (IHC)

Histological sections of COs were permeabilized in 0.2% Triton X-(Merck) in PBS and blocked in 2% normal goat serum (Merck) in permeabilization solution. Sections were incubated with primary antibodies diluted in the blocking solution at 4°C overnight and then with secondary antibodies for 1 h at room temperature (used antibodies are listed in Key Resources table). Nuclei were visualized by 4′,6-diamidino-2-phenylindole (DAPI; Carl Roth). Histological sections were imaged with an inverted microscope Zeiss Axio Observer.Z1 with confocal unit LSM 800 (Zeiss).

β-amyloid quantification

Aβ aggregates were visualized in paraffin sections by IHC and scanned by the fluorescent microscope TissueFAXS (TissueGnostics GmbH). For quantification, at least four microphotographs of one CO section were analyzed. At least four distant sections were evaluated for each CO, and two COs were sectioned per time point for each cell line used (NDC/AD#1, #2, and #3). The size of Aβ aggregates was analyzed by ImageJ software. According to the distribution of the size values of aggregates, the threshold was set to 20 pixels to remove the IHC background, and APP clusters larger than 100 pixels were considered as Aβ aggregates. The percentage of larger Aβ aggregates was counted for every section and plotted as an individual dot in the graph. Values were normalized to the average of the respective NDCs. Antibody used for APP detection is listed in the Key Resources table and was previously used and validated in.[9,12,70]

Whole-mount and CUBIC clearing

As described previously,[80] fixed organoids were incubated in a CUBIC1 reagent at 37°C for 5–7 days with one CUBIC1 reagent exchange (after 3 days). After incubation, samples were washed and blocked for 3–6 h at room temperature. Subsequently, samples were incubated with primary antibodies diluted in blocking buffer for four days at 4°C followed by washing and incubation with secondary antibodies and HOECHST 33342 (Thermo Fisher Scientific) for 24 h at 4°C. Next, samples were washed and incubated in a CUBIC2 reagent at room temperature for 24–36 h. All incubations were done while gently shaking. Cleared and stained organoids were embedded in mounting solution in μ-Slide 8 Well (IBIDI) for confocal microscopy (Zeiss Axio Observer.Z1 with confocal unit LSM 800; Zeiss) and in a cut 1 mL plastic syringe (BD Micro-fine) for light-sheet microscopy (Zeiss Lightsheet 7; Zeiss). All primary and secondary antibodies used are listed in the Key Resources table.

Whole-mount and CUBIC clearing buffer compositions

CUBIC1	25% urea (Merck), 25% N,N,N′,N′-Tetrakis(2-Hydroxypropyl)ethylene (Merck) and 15% Triton X-100
Washing buffer	0.5% Triton X-100 in PBS
Blocking buffer	PBS, 5% normal goat serum, 0.5% Triton X-100, 0.01% NaN3
CUBIC2	50% sucrose, 25% urea, 10% Triethanolamine (Merck) and 0.1% Triton X-100
Mounting solution	1% agarose in CUBIC2 and PBS 3:1

Microscopy

Samples of histological sections were imaged with the inverted microscope Zeiss Axio Observer.Z1 with confocal unit LSM 800, equipped with solid state lasers (405, 488, 561, 640 nm), using Plan-Neofluar 10x/0.30 AIR and Plan-Neofluar 20x/0.50 AIR objectives and ZEN Blue software (Zeiss). 1,437 x 1,437 pixel images with 0.222 × 0.222 × 2 μm (20x) and 0.45 × 0.45 × 4 μm (10x) pixel size were acquired using GaAsp PMT detectors and TPMT detector for transmission light detection. The acquisition parameters of detectors for Alexa Fluor 488, 568, and 647 were: 497,553 nm, 565,617 nm, and 656,700 nm (emission wavelength range) and 1.47 μs (pixel dwell time). Scan mode was set up to frame, and the pinhole was set to 1AU. Line average of 2 was applied to all channels.

Cleared whole-mount organoid D145 was also imaged with the inverted microscope Zeiss Axio Observer.Z1 with confocal unit LSM 800, using Plan-Neofluar 5x/0.16 AIR objective and ZEN Blue software (Zeiss). 2,867 x 2,867 pixel images with 1.248 × 1.248 × 14.66 μm pixel size were acquired using GaAsp PMT detectors. Alexa Fluor 568 and 647 acquisition parameters were: 565,617 nm, 656,700 nm (emission wavelength range), and 1.03 μs (pixel dwell time). Scan mode was set up to frame, and the pinhole was set to 1AU. Line average of 2 was applied to all channels. A total of 9 tile scans were acquired with 10% overlap.

Cleared whole-mount organoids D115 and D185 were imaged in CUBIC2 reagent (n = 1.457) with Zeiss Lightsheet 7, using 5x/0.1 foc illumination objective and 5x/0.16 foc detection objective n = 1.33–1.58, and using 10x/0.2 foc illumination objective and Clr Plan-Neofluar 20x/1.0 Corr detection objective n = 1.45 (Zeiss). For excitation of HOECHST 33342 and Alexa Fluor 568, 405 and 561 nm laser was used with a combination of the filter set DAPIGFP (BP 420–470 nm) and Cy3Cy5 (BP 575–615 nm). Samples were acquired with a 2x PCO edge 4.2 sCMOS camera controlled with ZEN Black software. The acquisition parameters were as follows: image size = 3,648 x 3648 (5x) and 5,376 x 5,376 px (20x), pixel size = 0.95 × 0.95 × 3.28 μm (5x, GM36 D117), 0.95 × 0.95 × 5 μm (5x GM26 D185) and 0.22 × 0.22 × 0.7 μm (20x), and illumination mode = dual (mean fused). For D115, the lightsheet thickness was set to 9.44 (5x) and 4.54 μm (20x). For D185, the light-sheet thickness was set to 8 (5x) and 4.2 μm (20x). Tile scans were acquired with 10% overlap.

z series were processed using the ZEN Blue software and displayed as maximum z projections. Gamma, brightness, contrast, and crop were adjusted using the ImageJ.[81]

Scanning electron microscopy (SEM)

Scanning electron microscopy was performed as described in.[82] Briefly, COs were fixed in 3% glutaraldehyde in 0.1 M cacodylate buffer overnight, washed with 0.1 M cacodylate buffer, and dehydrated through an increasing alcohol series (30-50-70-80-90-96-100% ethanol). COs were then dried in a critical point dryer (BAL-TEC Inc) using liquid CO_2 and sputtered with gold in a sputter coater (Balzers Union Limited). The scanning was done on an electron microscope (VEGA TS 5136 XM, Tescan Orsay Holding) using a secondary emission detector and a 20 kV acceleration voltage.

ELISA

For ELISA, individual COs were cultivated in Essential 6 Medium (Thermo Fisher Scientific) for 72 h prior to analysis. The cell culture medium and the corresponding organoid were collected and stored separately at −80°C. The amount of Aβ40 and Aβ42 peptides in the cell culture media was measured with Amyloid beta 40 Human ELISA Kit (Thermo Fisher Scientific) and Amyloid beta 42 Human ELISA Kit, Ultrasensitive (Thermo Fisher Scientific) according to the manufacturer's instructions. Samples were analyzed in technical duplicates. To compare the amounts of Aβ40 and Aβ42 peptides from organoids of different sizes, we measured the total protein concentration of lysed organoid, calculated total protein weight, and used it for normalization. Values represent pg of Aβ/μg of protein.

Proteomic analysis

Sample preparation workflow for mass spectrometry proteomics

For protein extraction, an optimized protocol was used as described in[77] with minor modifications. Briefly, COs harvested for selectedreaction monitoring (SRM)-MS analysis were washed with PBS, treated with a cell recovery solution (Corning) for 1 h at 4°C, and washed again with PBS. For multiplex protein analysis, a single CO was used. COs were lyophilized (Gamma 1–16 LSCplus, Martin Christ GmBH). Next, 100 μL of 80% IPA was added to the lyophilized COs with a glass bead to precipitate the protein pellet, then the sample was homogenized (BeadBlaster TM 24, Benchmark Scientific), vortexed (1 min), sonicated (37 Hz, 5 min), mixed (10 min, 2,000 rpm), centrifuged (5 min, 12,300 g), and the supernatant (85 μl) was removed. The protein pellets were dried (37°C, Savant SDP121 P, SpeedVac Vacuum Concentrator, Thermo Fisher Scientific) and processed using a proteolytic workflow for SRM protein assays. The dried protein pellets were solubilized in the ammonium bicarbonate (AmBic) buffer (50 mM) with sodium deoxycholate (SDC) detergent (5 mg/mL) as described in,[83] homogenized (4 m/s, 10 s, two cycles with 10 s inter-time), sonicated (1 min, 80 kHz) and mixed (10 min). After centrifugation (1 min, 12,300 g), 5 μL of supernatant was sampled for BCA assay to determine the total protein concentration in the sample that was then adjusted to 0.3 μg/μL. Samples (21 μg of protein) were reduced (20 mM DTT in 25 mM AmBic; 10 min; 95°C) and alkylated (40 mM IAA in 25 mM AmBic; 30 min; ambient temperature in the dark). Trypsin was added in the ratio of 1:40 (enzyme: total protein content, w/w), and the Parafilm -sealed samples were incubated (16 h; 37°C; gentle rocking). The enzymatic proteolysis was quenched with 200 μL of 2% FA. The samples were spiked with the isotopically labeled synthetic peptides (sample conc. ≈43.3 nmol/L) and loaded on the mixed-mode cartridge (Oasis PRiME HLB – 30 mg, Waters Corp. Milford) for solid-phase extraction (SPE): Peptides were washed with 300 μL 2% FA and eluted with 2 × 250 μL of 50% ACN with 2% FA. Purified digests were then dried in SpeedVac.

Mass spectrometry protein assays and data processing

Dry SPE purified peptides were reconstituted in20 μL of 5% ACN with 0.1% FA. Peptides were analyzed in positive ion detection mode using a UHPLC system (1290 Infinity II; Agilent Technologies) coupled to a triple quadrupole mass spectrometer (Agilent 6495B, Agilent Technologies) operated in SRM mode. A sample volume (3 μL) was injected on the C18 analytical column (CSH 1.7 μm, 2.1 mm × 100 mm, Waters Corporation, Milford). After sample injection on the analytical column, the mobile phase flow rate was 0.3 mL/min; buffer A (0.1% FA) and buffer B (0.1% FA in 95% ACN). Linear gradient elution: initial 5% B; 25 min 30%

B; 25.5 min 95% B; 30 min 95% B; and from 31 to 35 min with 5% B. The ESI source temperature was 200°C and sprayed voltage 3.5 kV. Multiplex SRM protein assays were designed as described in[84,85] using the neXtprot database (online, www.nextprot.org) to select 2–4 proteotypic peptides per protein. We preferred peptides with experimental evidence in the PeptideAtlas (online, http://www.peptideatlas.org). A list of SRM transitions (3–4 per peptide) was created in the SRMAtlas (www.srmatlas.org), and optimal collision energies were supplemented in Skyline software (21.1.0.146, MacCoss Lab, WA, USA) to generate a dynamic SRM acquisition method with a 2-min window centered at a peptide experimental retention time.[83] Data were manually inspected and processed in Skyline. Selected quantifier transitions per protein were used to determine relative concentrations (Table S3); light peptide peak area/ST peptide peak area*ST peptide concentration. Calculated protein amounts (ng) were normalized to the GAPDH levels (μg). The linear response of the quantifier standard peptides was checked using calibration points in the range of 5.4–433.3 nmol/L (in sample matrix). All the calibration points were processed the same way as the individual samples of COs and injected multiple times (n = 4–7) throughout the whole analysis of the individual. See also Table S3 with two Tables and respective Graphs.

Chemicals used for mass spectrometry proteomics

Ammonium bicarbonate (AmBic, BioUltra, ≥99.5%purity, 09830-500G), sodium deoxycholate (SDC, BioXtra, ≥98.0% purity, 30970-25G), iodoacetamide (IAA, ≥99% purity, I6125-5G) were from Merck. 1,4-dithiothreitol (DTT, ≥99% purity, Art.-Nr. 6908.1) was from Carl Roth GmbH. LC-MS grade acetonitrile (ACN, Cat# 34967), isopropanol (IPA, Cat# 34965), and formic acid (FA, for MS ~98% purity, Cat. 94318-250ML) were purchased from Honeywell. Trypsin gold, Mass Spec Grade, was obtained from Promega. Heavy labeled SpikeTides_L crude standards were synthesized by JPT Peptide Technologies Inc. Pierce BCA Protein Assay Kit reagents were from Thermo Fisher Scientific. The ultrapure water was obtained from the purification system (arium Comfort System, Sartorius).

Organoid Dissociation and scRNA-seq library construction

For each scRNA-seq sample, 18 COs were used. Whole organoids were washed in HBSS (Merck), cut into smaller pieces with a sterile scalpel, and dispersed into 250 μL/organoid of collagenase P (Merck) dissolved in HBSS at 0.5 mg/mL. Dissociation was performed in a shaking incubator for 15 min at 37°C with occasional pipetting using a 1 mL pipette, followed by 10-fold dilution with cold 2% FBS (Thermo Fischer Scientific) in HBSS and filtering through 40 μm cell strainer. Cells were collected by centrifugation at 300*g*, 4°C for 5 min and resuspended in 500 μL of 2% FBS in HBSS. The cell suspension was stained for viability with 7-AAD, and 500,000 viable cells were sorted using BD FACSAria Fusion cell sorter, and an aliquot of this suspension was used for library preparation.

Single-cell partitioning, cDNA preparation, and library construction were done using Chromium Next GEM Single Cell 3' Reagent Kits v3.1 (10x Genomics) according to the manufacturer's protocol. Quality control of the single-cell cDNAs and sequencing libraries was performed by a Fragment analyzer (DNF-474 High Sensitivity NGS Fragment Analysis Kit, Agilent Technologies). Libraries were pooled, and this pool was sequenced on NextSeq 500 (NextSeq 500/550 High Output 75 Cycles Kit v2.5; Illumina) using a 28 × 55 sequencing run format and producing about 200 million reads per library.

ScRNA-seq data processing and analysis

We used Cell Ranger 10x Genomics software (v 5.0.1) to perform alignment of the reads to the GRCh38 human genome assembly, filtering, barcode counting, and UMI counting with the default parameters. For further data processing, we applied Seurat[86] and excluded the cells with less than 1,000 or more than 7,000 detected genes and with mitochondrial gene proportion higher than 10%. We used a regularized negative binomial regression to normalize filtered data (using *SCTransform* function with default parameters) and performed principal component analysis (PCA) based on 3,000 genes with the highest residual variance. The clustering was conducted with the Seurat functions with default parameters using the top 15 principal components. After the clustering, we inspected cell quality on the cluster level. We identified and removed the cluster of the putatively stripped nuclei/damaged cells. Subsequently, we reprocessed data, regressed out the difference between S and G2/M cell cycle scores, and performed PCA and clustering. UMAP embedding was generated using the *RunUMAP* function with default parameters based on the top 15 principal components. We used a natural language processing concept of term frequency-inverse document frequency (tf-idf) to identify cluster-specific genes using the *quickMarkers* function from the SoupX R package.[87] To visualize marker genes on the UMAP embedding, we calculated and plotted gene-weighted kernel density using the *plot_density* function from the Nebulosa R package.[88] To compare our cells with published data, we performed similarity prediction using the SingleR R package.[89] We used a brain organoid scRNA-seq dataset from[28] as a reference dataset of samples with known labels.

The loompy (https://linnarssonlab.org/loompy/index.html)/kalisto[90] counting pipeline was used to estimate count matrices of unspliced and spliced abundances. To calculate and analyze RNA velocity, we used the dynamical model of the scVelo Python package.[91] To further characterize the cell fate decision process, we used the CellRank Python package.[92] We limited the analysis to neuronal and glial lineage containing intermediate states. Moreover, we excluded cycling cells as the interesting information is masked with a strong signal from genes regulating the cell cycle.

To secure the reproducibility of our analyses, we used Rmarkdown and WorkflowR R package[93] for R scripts and Jupyter Notebook for Python scripts. The reports with code can be found at https://petrsh.github.io/AD_CO_scRNAseq.

ScRNA-seq data integration and comparison of NDC#1 and AD#1

We used Cell Ranger 10x Genomics software (v 5.0.1) to aggregate datasets into a single feature-barcode matrix. We subsampled reads and subset the cells such that the datasets have the same effective sequencing depth and contain the same number of cells, respectively. To remove a putative batch effect, we applied the cluster similarity spectrum (CSS) method[94] that achieves integration by representing each cell by its transcriptome's similarity to every cell cluster in each sample. The clustering was conducted with the Seurat functions with resolution 0.4 using CSS representation. To analyze the proportional difference in cell populations between NDC#1 and AD#1, we calculated the significance of the difference by permutation testing using the scProportionTest R package.[95] We extracted cells of the neuronal lineage and inferred the developmental trajectory from progenitors to mature neurons using the Slingshot R package.[96]

QUANTIFICATION AND STATISTICAL ANALYSIS

Data analyses were done using GraphPad Prism version 8. Outliers were identified by the Grubbs method[97] ($\alpha = 0.01$) and removed from further analysis (a maximum of one outlier was removed per condition). Two-tailed Student's t-test was performed, and differences were considered statistically significant at $^{*}p < 0.05$, $^{**}p < 0.01$ and $^{***}p < 0.001$. All data are presented as mean and ±SEM and plotted as a bar graph with depicted individual values as dots. The number of samples per group (n) for each experiment is indicated either in the figure legend or in the Table S1.